FINITE ELEMENT ANALYSIS (FEA) STUDY OF THE THERMAL STRESS CONCENTRATIONS IN PLANAR-TYPE SODIUM SULFUR (NaS) SECONDARY BATTERIES

by

Jeffrey P. Colker Jr.

A Thesis Submitted in
Partial Fulfillment of the
Requirements for the Degree of

Master of Science
in Engineering

at

The University of Wisconsin-Milwaukee
December 2015

ABSTRACT

FINITE ELEMENT ANALYSIS (FEA) STUDY OF THE THERMAL STRESS CONCENTRATIONS IN PLANAR-TYPE SODIUM SULFUR (NaS) SECONDARY BATTERIES

by

Jeffrey P. Colker Jr.

The University of Wisconsin-Milwaukee 2015
Under the Supervision of Dr. Chang-Soo Kim

The importance of a reliable and safe way to store energy, and allow for on-demand usage, has led to much research in the field of secondary battery development. The thesis herein explores a technology that has shown promising results when implemented in large-scale energy grid applications. Though the technology has proven viable in both load-leveling on existing grids as well as serving to legitimize renewable energy sources, the development of such advanced battery systems is not without challenge. Sodium-sulfur (NaS) secondary cells have shown promising results when implemented in the aforementioned energy storage applications. One of the main drawbacks to this technology however, is that the cells must operate at elevated temperatures (~350°C) for facile transport of active materials. The high operating temperatures keep the highly reactive molten electrodes in the liquid phase, which can lead to catastrophic failure if not properly contained. This has led much research in the direction of safety advancements while maintaining the overall desired cell output efficiency. The complexity of the thermal loading conditions induced during the production sequence and subsequent operation has made successful

development both difficult and expense. In particular, the stress accumulation in the cell joint areas are of high concern. Through the incorporation of finite element analysis (FEA), the complexities of the intricate cell design, and influences from thermomechanical stresses can be studied more easily. In this work, several computational models of the cell have been developed to predict the thermally induced stress concentrations on the various components within the planar-type NaS cell. The ABAQUS commercial software package (Hibbit Karlson & Sorences Inc. Pawtucket, RI, USA) was implemented to perform the computational analyzes. Throughout the current work, the impacts of geometrical and material specific properties were modified to quantify the impacts of those variables on the resultant stress accumulations. The development of the current models can be used to accurately predict the relative induced motions of the dissimilar materials within the cell. From the results, the highest thermal stress concentration areas, with corresponding stress values in the cell, were predicted. Additionally, by modifying the coefficients of thermal expansion (CTE) values of the various materials; the resultant normal and shear stress concentrations during temperature cycling were investigated. It is anticipated that the developed computational model can be readily applied to select the constituent materials and to optimize the cell design toward enhanced stability and safety.

DEDICATIONS

The work herein is dedicated to all of those that supported me both consciously and unconsciously throughout this exhausting process. You know who you are, and I cannot thank you enough. You have truly helped to positively shape my future.

TABLE OF CONTENTS

LIST OF FIGURES

LIST OF TABLES

LIST OF ABBREVIATIONS

NaS	Sodium-sulfur secondary cell
FEA	Finite elements analysis
ESS	Electromechanical storage systems
BASE	Beta-alumina solid electrolyte
EV	Electric vehicle
CTE	Coefficient of thermal expansion
FEM	Finite element method
2D	Two-dimensional
3D	Three-dimensional
DoD	Depth of discharge
XRD	X-ray diffraction
K	Boltzmann constant
Å	Angstrom
µm	Micrometer
J/K	Joules per Kelvin
TCB	Thermal compression bonding
Tg	Glass transition temperature
Ts	Glass softening temperature
RIST	Research Institute of Industrial Science and Technology
mm	millimeter
Al	Aluminum
STS	Stainless steel
CPU	Central processing unit
TD	Temperature dependent
MoE	Modulus of elasticity
ASM	American Society for Metals
UNS	Unified numbering system
AISI	American Iron and Steel Institute
wt%	weight percent
MPa	Mega-Pascal
K^{-1}	per Kelvin
°C	Degrees Celsius
IH	Insulating header
IM1	Upper insert metal
IM2	Lower insert metal
GS	Glass-Sealing

ACKNOWLEDGMENTS

I would first like to acknowledge Dr. Chang-Soo Kim for his tireless efforts in aiding me to complete this work. Dr. Kim was an inspiration since the topic was first introduced, and gave all he could to see this work through completion. I would also like to formally acknowledge both my family and friends for their never ending enthusiasm and encouragement when I needed it most. A special thanks goes out to Mr. Yuzhe Cao as well, I could not have completed this work without you!

Thank You All.

Chapter 1 – Introduction

1.1 Overview

The constant increasing demand for reliable energy, paired with the forecast for incremental increases in the prices of fossil fuels, will no doubt force the implementation of new technologies that can both economically and safely store large concentrations of energy when it is prevalent, and release said energy upon demand. Countless attempts to harness relevant reserves of collected energy for later usage have thus far been futile. The current power generation grid of most developed regions requires constant monitoring and instantaneous adaptation in order to accommodate the inconsistent and many times cyclic demand. Therefore, an energy storage technology that can adequately address the spontaneous needs of the consumer, while exploiting renewable "clean energy" sources, is vital for future generations. The sodium-sulfur (NaS) secondary battery has received strong attention as one of the candidates for these large electrochemical storage systems (ESS). The work herein provides a discussion concerning an early solution to concerns, while contributing to the future development of related technologies implementing NaS battery applications.

The initial chapter will give a general introduction of the topic, personal motivations, and will formally address the proposed objectives of the research that follows. This first portion includes a brief preface for the NaS secondary energy cell, which will be further elaborated on in the second chapter, while also providing a general introduction to computer-aided finite element analysis (FEA).

1.1.1 The Sodium Sulfur Secondary-Cell (NaS Cell)

The sodium-sulfur cell, generally referred to as a "NaS" cell, is an electrochemical secondary battery that utilizes a solid electrolyte and two liquid electrodes. To ensure the sodium and sulfur electrodes remain in the molten state during operation, the cell must operate at elevated temperatures. Though the solidification temperatures of the two electrode metals and the readily formed sodium polysulfide (Na_2S_x, x = ~3-5) reaction products must be exceeded, it is the increased solid electrolyte ion-permeability that most heavily influences the desired average operating temperature of approximately 350°C [1, 2]. Fluctuations between 300 and 350°C are typical at different states of charge/discharge, based on the instantaneous electrochemical reactions and resultant products present within the cell [2]. Although countless attempts have been made in an effort to reduce the operating temperature of the NaS cell, increased stability and a reduction in safety concerns have until this point been only limited [3, 4, 5].

1.1.2 NaS Historical Perspective

Contrary to the preceding heavier and less energy dense lead-acid secondary cells, first discovered by French Physicists Gaston Planté in 1859 [1], the electrolyte of the NaS cell is in the solid state. This requires a unique material that allows for accelerated Na^+ ion permeability, while simultaneously blocking both electron passage and liquid leakage. The material must also exhibit a suitable resistance to both mechanical and thermal shock. The material used for the solid phase electrolyte is a binary spinal ceramic known as β-alumina, or BASE (i.e., beta-alumina solid electrolyte).

It is widely known that J. T. Kummer & N. Weber [1] of the Ford Motor Company are credited with the initial discovery of this material and the associated implementation of the NaS battery technology as early as 1967. The BASE corrosion resistance to the harsh molten electrodes and adequate mechanical strength make it superior to other thin walled glass capillary electrolyte options, which were under simultaneous development by Levine and Brown at the Dow Chemical Company [1, 6].

Although initially introduced by Kummer and Weber in the hopes of creating the first zero-emissions electric vehicle (EV), the unique characteristics of the NaS cell technology, and its ability to be easily linked with additional adjacent cells, makes the resultant cumulative batteries particularly attractive for mid to large-scale power grid applications [2, 7]. The current and potential future applications of these cells in large battery arrays include load leveling, peak shaving, and the incorporation of renewable energy sources for new and existing power grids worldwide. By accepting excess energy when available (i.e., charging), and releasing stored energy upon demand, (i.e., discharging) the cell is poised to make a dramatic difference in the worlds potential energy storage and usage capabilities.

1.1.3 Current Status and Research Interests

This idealized implementation is of course not without challenges. Some of the major areas of current research include premature breakage prevention of the delicate ceramic components, the minimization of the possibility of leakage and fracture at the glass-sealing location, and the improved corrosion resistance for the various containment materials. Within these broad topics of current exploration, much research is being performed in hopes of improving the current NaS cells and incorporating them on an even larger scale.

NGK Insulators, Ltd. (Japan), owned and operated by Tokyo Electric Power Company (Japan), is regarded as an early adopter of large-scale NaS implementations, and as of late 2013, their devices were in service in numerous countries on three continents, including nine large-scale installations in North America [7]. Initial shipments of the traditional NaS technology implementing cells began in 2002. These installations provide much needed load-leveling capabilities, as well as further legitimizing wind, solar, and other renewable energy technology integrations. NGK also hopes to integrate systems for smaller "micro-grid" applications where the installations, along with renewable energy technologies, can be used independent of existing grid methods [7]. The installations to date by NGK have been generally without incident, save for a single instance in September of 2011, where a 2,000-kW NaS battery array caught fire at the Mitsubishi Materials Corporation site in Joso City, Japan [8]. Although the large-scale fire did compromise several individual cells, safety precautions in the batteries design prevented catastrophic failure of the entire system. NGK formally apologized for the incident, and vowed deep regrets to their client, local authorities, and residents in the area [8]. Generally speaking, NGK NaS implementations have thus far gone without any other major documented incidents.

1.1.4 Tubular vs. Planar Cell Geometries

To date, two dominating cell geometries have been extensively researched. The more traditional geometry is referred to as "tubular" and is currently operating globally with much success. The majority of the more recent research however favors a new "planar" type cell design. For visual comparison, representative schematics of the two common cell geometries are presented in Figures 1.1 and 1.2. As shown, both cells exhibit the characteristic dual

molten electrode chambers, solid BASE separator, intricate glass-sealing areas, and outer metallic case. Although the tubular cells can be installed in either a vertical or horizontal orientation, the vertical has been largely accepted due to the high feasibility of manufacturing larger cells with reduced emphasis on sealing concerns. In the tubular-type horizontal orientation, contact of the sealing materials with the highly corrosive molten electrodes cannot be avoided, thus, most of the practical tubular cells are based on the vertical orientation configuration.

One of the main disadvantages of the tubular cell design is the fabrication of the thin-walled elongated hollow ceramic electrolyte tubes. It is essential that the thickness of the brittle ceramic be uniform along its length. Any dimensional inconsistencies can lead to localized charge build-ups, hindering the overall individual cell performance, and possibly contributing to premature failure during operation [1].

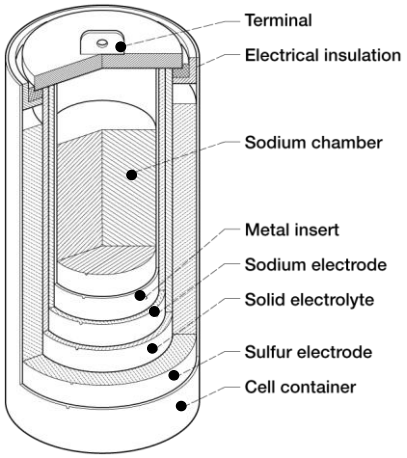

Fig. 1.1-Typical tubular-type cell geometry with the main components identified [9].

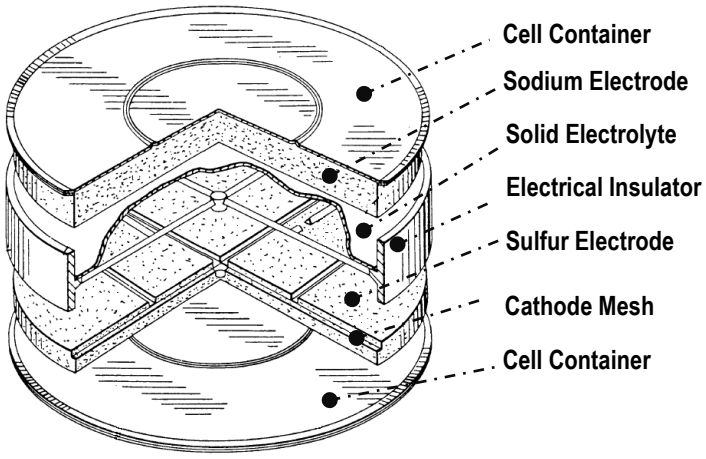

Fig. 1.2-Typical planar-type cell geometry with the main components identified [10].

On the other hand, planar-type cell designs require only a circular shaped thin wafer or disk that is easily mass-produced, and improves the surface interaction area of the electrolyte with the two electrodes, for comparable cell volumes. Planar cells can also be more easily arranged in a bipolar array, eliminating the need for external cellular connections that are required for the tubular cell assemblies [1]. It is also important to note that the cell geometry of the tubular cells allow for varying reaction rates in the radial direction, which can easily promote cell degradation, and reduce the performance of these cells. In the planar cell, the volume of the molten electrode to electrolyte surface area ratio is increased, decreasing the cell resistance obtained upon discharge. In the tubular cell, the diffusion/transport kinetics of Na^+ ions, liquid sulfur, and sodium polysulfides could be uneven along the radial direction of the cell because of the inherent tubular geometry. This can lead to the accumulation of the higher resistance, lower stoichiometric liquid polysulfides and eventual solids, which may deteriorate the cell performance as well [11].

Additional concerns with the planar cell types do however exist. The major issue is associated with the larger size of sealing area that would be subject to higher thermomechanical stress concentrations, during the cell assembly and operation, due to the substantial differences in the coefficients of thermal expansion (CTE) between the constituent sealing components (glass, BASE, and metals) [1]. The active electrolyte area in similar volume cells is higher for the planar cell geometries, however, like the horizontal tubular cell orientation, requires the entire seal location be submersed in the highly corrosive electrode metals. In addition, early stage prototyping has also identified centering of the BASE disk in the glass-sealing as an utmost concern. Any deviation from absolute center will induce inconsistent stresses in the glass-sealing material and mating components, leading to premature failure.

The available documentation regarding planar cell development has mainly focused on circular geometries to this point; however, square, hexagonal, and other polygon-shaped designs with rounded corners are gaining attention. These cells offer a higher packing density when considering the total assembled battery footprint, and leave uniform repeating compartments surrounding the cells, which allow space for the required thermal management system and uniform insulation.

1.2 Finite Element Analysis (FEA)

FEA, regularly referred to as the finite element method (FEM), is a widely respected computational approach for predicting the naturally occurring mechanical behaviors of complicated two and three-dimensional (2D and 3D) aggregates, that would otherwise be extremely difficult or even impossible. By mathematically representing complex continuum,

the resulting simulations based upon interactions between individual architectural segments can be scrutinized. A variety of proposed interactions and the resulting events can be modeled using the FEA approach. Common areas of interest include force, displacement, and point pressures, thermal heat flux modeling, and a multitude of stress-strain analyzes based on various static and dynamic loading situations [12].

1.2.1 FEA Historical Perspective

The fundamental development of FEA principles is said to go back as far as the early Greek Philosophers, and in more modern times is typically employed by Physicists, Mathematicians, and Engineers across many fields of interest [12]. R. Courant, who utilized the Ritz method of numerical analysis and minimization of differential calculus to obtain approximate solutions to vibrational systems, [13] is thought of as formally developing the field of FEA in 1943. Shortly following, a paper published in 1956 by M. J. Turner, R. W. Clough, H. C. Martin, and L. J. Topp, [14] established a broader definition of numerical analysis. This particular work focused on the "stiffness and deflection of complex structural members" [12 - 14].

By the late 1970's, FEA modeling was only accessible to those with large mainframe computer access, which limited the legitimate implementation to fields such as aeronautics, automotive, defense, and nuclear industries [13]. It was not until the technological surge of the late 20th and early 21st centuries that it became possible for individual users to fully benefit from FEA techniques. Currently, FEA is regularly employed for more complex situations incorporating fluid flow, heat flux, electromagnetic fields, soil mechanics, acoustics, and biomechanics applications in a multitude of disciplines [12]. FEA software

provides a wide range of simulation options and methodologies for controlling the desired level of accuracy required, while considering the associated computational time constants.

During structural simulations, FEA can be a visual guide to illustrate where higher stress regions are located, as well as aiding in the optimization and selection of materials containing the required properties. FEA allows for a visualization of where a structure is likely to encounter physical movements and distortions, or indicating where bending or torsional loads will be confined, based upon carefully controlled boundary conditions. All of these considerations are developed in an effort to produce a more robust cost effective design, while reducing the time and resources used in traditional prototype development, and time to market. Specifics chosen in this work will be thoroughly discussed as it pertains to the NaS cells under investigation. Beyond strictly development, FEA is routinely used for product optimization and the always-popular cost reduction justifications on existing products. Direct benefits of FEA implementation include the identification of critical design parameters, virtual prototyping, a generally quicker and less costly design cycle, elevated productivity, and subsequent increased revenue.

1.2.2 FEA Model Development Overview

Successful FEA executions depend heavily upon the development of realistic numerical representations of the actual components under investigation. Predefined material properties for individual constituents, and quality representations of the sub-assemblies must be made to accurately portray the represented tangible items. Both 2D and 3D models are used, based on the required accuracy of the predicted results. Although 2D models are generally considered less accurate, they are routinely implemented due to their

lower complexity and decreased computational resources, time, and complexity, as compared with 3D geometry models.

The modeling process begins by the dissection of larger continuum components into smaller finite sections called “elements.” Differential equations performed at each element are then extrapolated to the intersections of neighboring elements. These intersection sites are referred to as “nodes,” and form the basis for an overall spider-web like joining sites, which model the physical characteristics of the parts being portrayed [13]. The developed web of representative nodes is referred to as a “mesh.” The mesh of developed vectors between the adjacent nodes is what carries the specified material properties of the actual components of the assembly, which are used to predict how the specific elements will react under certain predefined loading conditions [13]. The closer the representative mesh mimics the actual parts, the more realistic the obtained results will be. It is therefore a common trade-off between the miniaturization of the associated web elements and the resulting computational times, which rise with the increasing number of nodes [12]. Therefore, it is necessary to assign varying densities of nodal concentrations to different components based upon the anticipated stress levels for each component.

Generally speaking, a higher nodal density is used for components and surfaces which are thought to have higher or more complex loading, while a larger less intricate mesh can be used to accurately portray less complex areas of the subject assembly. Geometric stress concentrations will by this theory carry a higher density than areas that are anticipated to stay more rigid during the simulations [12, 13]. Specifics concerning the thought process and techniques used to assign the working meshes for the various components of the NaS system used for this work, will be fully outlined in Chapter 3-Model Development.

1.3 Motivations

The successful implementation of NaS cells is of obvious importance; however, the process of designing, developing, and implementing these cells is not without challenge. In addition to the already demanding ceramic syntheses, intricate assembly processes, and the essential electrical operation; induced temperature changes and the associated resultant thermomechanical stresses are highly complex. Arising from dissimilar material types routinely subjected to similar but gradient temperature fluctuations, these induced stresses cannot be ignored during design. Seemingly unpredictable, these stresses and resultant mechanical deformations can be further understood using FEA simulation.

The majority of the production issues plaguing the current planar-cell types involve thermally induced failures, a direct result of mismatches in the respected CTE values. As mentioned previously, cracking or complete breakage of the ceramic components and glass-sealing fracture, are major causes for concern. Dissimilar metallic fit issues are routinely encountered as well. Experiment-based empirical trial-and-error has proven costly in terms of development overhead, processing, and time to market. It is important to note that increasing the cell size is a vital focus for the production of commercial NaS applications by reducing the manufacturing cost with competitive cell capacity. However, as the size of the planar NaS system increases, the resultant thermomechanical stress concentration in the sealing area increase as well, due to the aforementioned CTE differences between the various types of construction materials.

To date, FEA modeling has proven a powerful computational tool for improving all types of engineering applications, without the use of sometimes-scarce resources. The introduction of FEA has therefore substantially reduced the amount of time between

conception and production. FEA has incorporated thermally induced stresses between dissimilar material types for decades, and is highly regarded as an accurate method for simulating thermally dependent design considerations. Taking these advantages into account, the following work will employ advanced FEA modeling techniques to enhance the understanding of the resulting temperature induced mechanical behaviors.

It is known that fluctuations in temperature are maximized during assembly and implementation, as well as during maintenance intervals and eventual decommission. These vast changes in temperature and associated thermal strains give rise to several extreme cycles that must be considered. The details of the computational method will be fully addressed in Chapter 3, Computational Model Development.

1.4 Research Objectives

The proposed objectives of the current research aim to address several of the previously stated performance hindering factors as they relate to the unavoidable temperature fluctuations that are experienced by NaS cells under current development. Specifically, the stated objective of this thesis is therefore:

- To interpret the various induced thermomechanical responses within the planar-type NaS cell, when subjected to established temperature cycling during both fabrication and assembly, as well as normal operating conditions; using advanced computational FEA modeling techniques.

Given the known weaknesses at the various sealing and dissimilar material bonding interfaces, the necessary physical and thermal properties of the metallic, ceramic, and glass portions of the cell will be thoroughly discussed. These unique material types and resulting interactions make it particularly difficult to predict the various performances of the total assemblies during nearly uniform heating and cooling cycles. In particular, we will focus on the impacts of the following cell constituent material types and designs on the resultant accumulation of thermomechanical stress.

- CTE of glass-sealing
- CTE of the stainless steel cell container
- Thickness of insert metals
- Thickness of the stainless steel container case
- Symmetry of the electrolyte in the planar-type cell

Though the main focus is on determining where the greatest stresses are induced during temperature cycling, the model developed can also be used to investigate proposed material changes investigated during initial trials. Proposed design implementations and recommendations for improved cell geometries will also be expressed in an effort to aid in the development of future cells. The immediately following (Chapters 2 and 3) will expand upon the introduced NaS cell background, as well as to establish the psyche behind the cumulative representative finite element models developed during the simulation process. Chapter 4 will then present the results of the computations, including thorough discussion, before Chapter 5 summarizes the work, including future directions and limitations.

Chapter 1 References Cited

1. J. L. Sudworth and A. R. Tilley, *The Sodium Sulphur Battery,* London: Chapman & Hall, pp. 5-13. 1985.

2. K. Jung, S. Lee, Y. C. Park, and C. S. Kim, Power Sources, vol. 250 (2014), pp. 1-14.

3. T. B. Kim, J. W. Choi, H. S. Ryu, G. B. Cho, K. W. Kim, J. H. Ahn, K. K. Cho, H. J. Ahn, Journal of Power Sources, vol. 174 (2007) pp. 12-75, 1278.

4. X. Lu, W. Xu, G. Li, J. Y. Kim, J. P. Lemmon, V. L. Sprenkle, and Z. Yang, Energy Environmental Science, vol. 6, (2013) pp. & 299-306.

5. J. Wang, J. Yang, Y. Nuli, R. Holze, Electrochemical Community, vol. 9, (2007), pp. 31-34.

6. Y. F. Yao, and J. T. Kummer, Journal of Inorganic Nuclear Chemistry, vol. 29, (1967), pg. 2453.

7. NGK Insulators, Ltd., NaS Battery Energy Storage System. Edison Electric Institute Press Release: May, 2013.

8. K. Taro, S. Sakabe, NaS Battery Fire Incident and Response. October 28, 2011.

9. N. McDonald, Sodium Sulfur Battery. Center for Environment, Commerce & Energy. Nov. 2012.

10. G. Landis, and J. Glenn, Research Center. PD-USGOV-NASA. July, 2008.

11. Sernka et al., US Patent No, Oct. 1, 1991, 5,053,294.

12. B. Wah, "The Finite Element Method." *Wiley Encyclopedia of Computer Science and Engineering*. John Wiley & Sons, Inc. (2008).

13. P. Widas, Introduction to Finite Element Analysis. Virginia Tech Material Science and Engineering. (1997).

14. M. J. Turner, R. W. Clough, H. C. Martin, and L. J. Topp, "Stiffness and deflection analysis of complex structures." J. Aeronaut. Sci., vol. 23 (1956) pp. 805–823.

Chapter 2 – NaS Cell Background

The NaS cell is highly regarded for its ability to achieve high current densities during discharge, high charge acceptance during charging [1], an overall low cell resistance [2], and the incorporation of ubiquitous low cost raw materials [3]. Other advantages include long discharge time (up to eight hours at full power [4]), high-energy capacity (up to larger than 1200Wh per cell [4]), long lifetime (over 15 years [5]), and high specific and volumetric energy capacity (222 Wh/kg and 367 Wh/L [6]). This chapter aims to establish the basic operation and construction of the cell by introducing the more important components within. The section opens with discussion of the operation specifics, and continues by describing several of the more important components of the NaS cell, and how they are combined during assembly.

2.1 General Cell Operation

During discharge the oxidized Na^+ ions sourced from the negatively charged cathode pass through the solid BASE electrolyte and arrive at the electrolyte-sulfur boundary in the positively charged sulfur anode. In this compartment, reduction of the molten sulfur occurs, producing various sodium polysulfides of which preferred stoichiometry are based upon the cells depth of discharge (DoD). The cell reactions during discharge are typically noted as stated below, where x =~2 - 5.

Oxidation at cathode (-):	$\mathbf{2Na \longrightarrow 2Na^{+} + 2e^{-}}$	**(EQ. 1)**
Reduction at the anode (+):	$\mathbf{xS + 3e^{-} \longrightarrow S_x^{2-}}$	**(EQ. 2)**
Resulting Net Reaction:	$\mathbf{2Na + xS \longrightarrow Na_2S_x}$	**(EQ. 3)**

The reverse is also true during the charging cycle. The reactions are completely reversible, and besides the possibility for degradation of the electrolyte over time, these cells do not typically suffer from memory effects encountered in most other secondary cells [1]. Additionally, high output efficiencies are obtainable due to the fully reversible internal cell reactions. Most of the literature points to an overall cell efficiency of 85 – 90% and a theoretically calculated specific energy of 760 W-h/kg, based upon the average net reaction shown above (EQ. 3), where again, x =~2 – 5 [1, 6, 7].

As stated, the NaS cells typical operating range is between 300 and 350°C, which according to the phase diagram shown in Figure 2.1, accounts for the formation of several two-phase immiscible regions as the wt.% pure $S_{(l)}$ is continually reduced during discharge. As shown in Figure 2.1, various stoichiometric liquid-phase sodium polysulfides are formed based upon the instantaneous DoD.

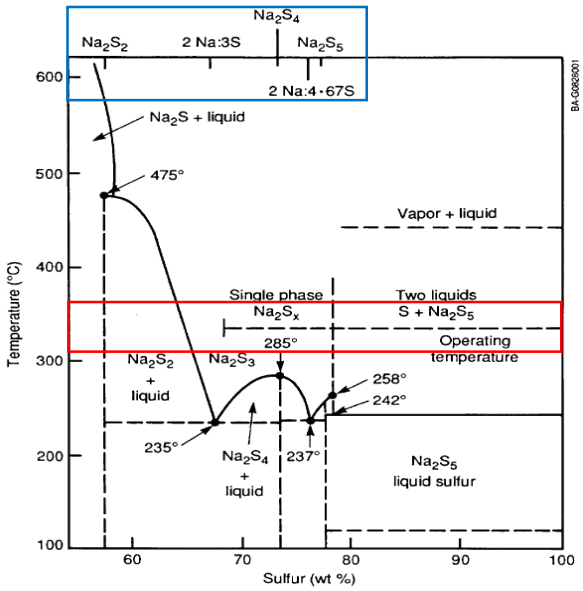

Fig. 2.1-The Na_2S-S phase diagram developed by Ohi (1972[6]) & Gupta & Tischer (1972 [7]). The red box shows the typical cell operation temperature range, while the upper blue box shows the various immiscible sodium polysulfides that are formed upon discharge (moving right to left in the diagram).

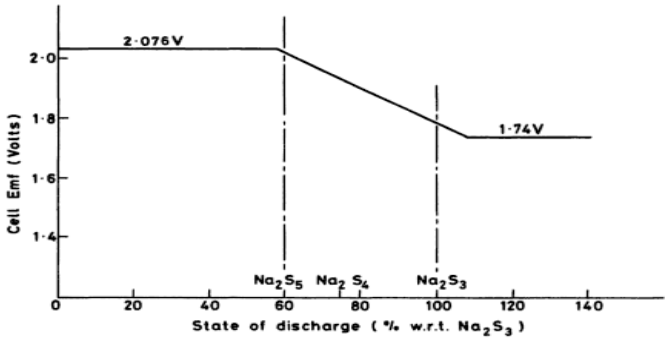

Fig. 2.2-The NaS cell EMF output as a function of depth of discharge (DoD) at 350°C (discharge, moving left to right) [1].

Moving right to left in the phase diagram (discharge), it is clear that a two-phase liquid is present until 78 wt. % sulfur is reached. The two phases prior to reaching this composition are $Na_2S_{5.2}$ and a nearly pure sulfur liquid [1, 6, 7]. The cell EMF through this percent

discharge was obtained experimentally, and is generally accepted as 2.076 V [1, 7]. Upon further discharge below 78 wt. % retained sulfur liquid, additional ionic sodium polysulfides form, with a resulting lower cell EMF, as shown in Figure 2.1 [1]. It was determined experimentally at 350°C by Gupta and Tischer (1972 [7]), and summarized by Sudworth (1983 [1]), when the new sodium polysulfides begin to form with progressing discharge, the EMF reduces linearly to 1.74 V; at which point, in the operating temperature range, the final liquid phase $Na_2S_{2.7}$ is formed.

Continuing to the left in Figure 2.1, within the illustrated operating temperature range, the initial solidus line is reached near a composition of approximately 65 - 68-wt. % sulfur. At this state of discharge, a two phase region of solid $Na_2S_{2.7}$ and a liquid sodium polysulfide melt ($Na_2S_{x(l)}$) coexist. Analyzing Figure 2.2 further, allows one to notice that the cell EMF plateaus again at 1.74 V, as long as a liquid phase is retained. It is here, or prior to this compositional region, where the NaS cell is ideally recharged, avoiding the formation of the solid $Na_2S_{2.7}$ phase.

2.2 The Beta-Alumina Solid Electrolyte (BASE)

It is understood that the successful advent of the NaS cell is a direct consequence of the discovery of the unmatched high ionic conductivity of sodium ions in the BASE ceramic oxide [8]. Though initially documented as early as 1916 (Rankin and Merwin [9]), it was not until the advent and proper application of X-ray diffraction (XRD) techniques that the ceramic was correctly characterized as a sodium-aluminum oxide (Bragg et. al., 1931 [10]). Bragg proposed an initial chemical formula of $Na_2O_311Al_2O_3$ [10]. It is now widely accepted that the β-alumina structure is never stoichiometric as prepared, and a less specific formula of $(Na_2O)_{1+x}11Al_2O_3$, (where x = ~0.25-0.66) is likely more accurate [11, 12].

The main factor contributing to the overall output performance of the NaS cell is the internal cell resistance; and the main contributing factor in reducing said resistance, is the β-alumina fast ion conductor. The essential electrolyte requirements include good ionic conductivity, zero electronic conduction, chemical resistance and physical impermeability of the reactants, as well as adequate mechanical strength [1]. The crystal structure is the most unique and important characteristic of the electrolyte and will therefore be discussed first.

2.2.1 Crystal Structure

Two main forms of β-alumina are formed during synthesis, namely β'- and β"-alumina. The unique crystal structures of each are of particular importance in allowing for the required fast Na^+ ion conduction. The parent electrolyte crystal structure is composed of alternating slabs of close packed oxides, and layers with low atom density containing cations (typically Na [1]). The close packed oxide layers accommodate small metal cations (typically Al^{3+}) in both octahedral and tetrahedral interstices, but not in the same proportion as in the spinal ($MgAl_2O_4$) [1].

As stated, there are two main crystal structures present in the final synthesized BASE. These include β'-alumina and β"-alumina. As shown in Figure 2.3a, the β'-alumina structure consists of a twofold screw axis containing a mirror plane through the layers of mobile cations, and results in a hexagonal crystal structure [1]. Close packed oxide layers extend normally to the hexagonal c-axis and adjacent slabs are held apart by rigid Al-O-Al spacer units. The characteristic ionic diffusion occurs exclusively within the open planes perpendicular to the c-axis [1].

The β”-alumina structure, on the other hand, exhibits a trifold screw axis with no mirror planes, and a rhombohedral shape, as shown in Figure 2.3b. Closed packed oxide layers are again held apart by Al-O-Al spacer units; however, in this structure, Na atom sites lie above and below the plane through the center of the oxide spacer atoms, and the Na^+ ion diffusion path encompasses a finite volume (the conduction slab) rather than a plane as in the β’-alumina structure [1]. The β”-alumina structure therefore exhibits a 50% larger unit cell due to the difference in stacking sequence, accounting for its higher Na^+ ion permeability.

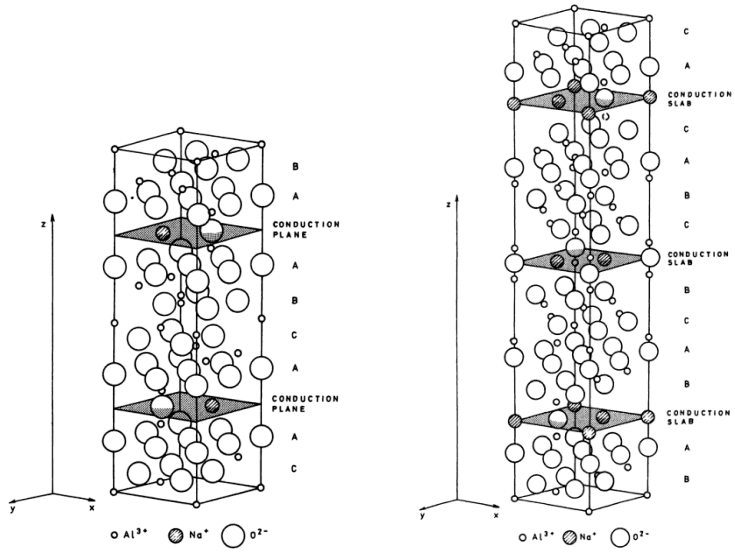

(a) **(b)**

Fig. 2.3-Schematic of the idealized *β’-alumina* **(a)** and *β”-alumina* **(b)** structures. The characteristic Na^+ ion conduction planes are shown. [1].

2.2.2 Crystal Defects

Many crystal defects are present in the final sintered product, which can seriously hinder the anticipated ionic conduction of the BASE. Defects found in the crystal structure of Mg doped β"-alumina tend to block the sodium ion conducting planes. These defects are difficult to study however, without inducing additional similar defects during analysis [1]. Grain boundary structures can also greatly affect the resistivity of the electrolyte as well. A key factor in determining the effect of grain boundaries on resistivity is whether or not the dislocations can accommodate the orientation mismatch [1]. If not, the resultant ion conduction is greatly reduced.

2.2.3 Composition and Phase Relationships

The β/β"-alumina structures are remarkable not only for their ionic conductivities but also for their versatility for isomorphous replacement. There is little in the typically quoted stoichiometry of $(Na_20)_{1+x}11Al_2O_3$ (x= ~0.25–0.66) which cannot be substituted by alternative ions [1, 11, 12]. The functions of additives in stabilizing one β/β"-alumina phase depend on their inclusion into the structure during sintering [1]. The limitations of cation substitutions in place of the Al^{3+} spinal block (mainly Li^+) is primarily restricted by size. Impurity cations larger than 0.97Å in radius can impede the conduction planes, however, and lower the intended migration rate of the Na^+ ions [13].

2.2.4 Sodium Ion Diffusion

As expected, ion diffusion through the electrolyte is thermally activated, and therefore, generally controlled by the classic diffusion coefficient shown below.

$$D = n_o \exp^{(-E/kT)} \qquad \text{(EQ. 4)}$$

Where $\mathbf{n}_o$ is the approach frequency, E is the activation energy required (in [J]), k is the Boltzmann constant (1.380 x 10^{-23} J/K), and T is the absolute temperature in Kelvin, respectively [1]. It is important to note that the actual diffusion rate is of course influenced by the specific composition and grain size/orientation of the electrolyte, however, generally follows the above equation [1, 14]. As expressed by the equation, an increase in temperature increases the ion conductivity (by reducing the negative exponent term), which has been verified experimentally by many [14 – 16]. The ideal region where the ion conductivity is sufficient for the intended NaS cell operation is reached at a temperature of approximately 350°C [1]. Minimal gain is experienced with further temperature increase, which is why the cell it is typically operated in the range of about 300 - 350°C [1, 15, 16]. Specific properties of the BASE will be further discussed in this chapter, as well as the model development chapter (Chapter 3).

2.3 The Sodium Electrode (Anode)

The sodium electrode is the electrode chamber where the molten elemental sodium is oxidized during the discharge cycle. A single oxidation reaction (EQ. 1) forms a Na^+ ion that is passed through the BASE to the sodium electrode, and releases a single electron through the adjoining circuit. Choice of containment materials is of major concern due to the highly corrosive nature of the molten electrode. Two additional requirements must be satisfied in order for proper operation of the cell to be maintained.

First, the sodium melt must remain in full contact with the entire interface of the solid electrode during both the charge and discharge cycles to prevent interfacial polarization [1].

This seems trivial, however the volume changes of the sodium electrode upon cycling can make this requirement especially difficult to maintain. Although gravity-fed designs are employed for vertical tubular cells, a more complex solution is required for planar type cells. Typically an additional partial partition, referred to as a cartridge, is implemented to account for the volume change. The use of the cartridge insures constant and complete wetting of the sodium melt with the BASE. The construction specifics will be elaborated on in the model development chapter (Chapter 3).

Good wetting in the anode regions is also an important factor in determining the cell performance. Early stage development studies conducted by Gibson (1977 [19]) investigated the wetting of liquid sodium on the electrolyte surface. These studies revealed that polished electrolyte surfaces significantly decreased the occurrence of resultant interfacial polarization [19]. More recent work has confirmed the initial conclusions, that proper wetting can significantly decrease both the interfacial polarization, as well as decrease the overall resultant cell resistance [20, 21]. Additionally, it was proven that reduction or elimination of retained moisture present in the fabricated BASE can significantly increase proper wetting of the surface, resulting in less risk of interfacial polarization in the sodium cathode.

2.4 The Sulfur Electrode (Cathode)

The sulfur electrode is the compartment where the molten elemental sulfur is reduced to the various sodium polysulfides during the discharge cycle. The various sodium polysulfide compounds must then be reversibly oxidized upon charging [1]. Although little complication is encountered during the entirety of the discharge cycle, the formation of

insulating liquid sulfur in the two-phase solution significantly hinders the electrical conduction during the charging cycle [1]. Due to the insulating nature of the liquid-phase elemental sulfur ($S_{(l)}$), the presence of an electronic conductor in the sulfur electrode compartment is required for the essential electron transfer.

The cathode material is one of the most influential components to determine the charge/discharge characteristics of NaS batteries. The liquid sulfur is typically immersed in the cathode felt (comprised of carbon and glass fibers) that allows facile transport of electrons and poly-sodium sulfides (i.e., Na_2S_x). Upon discharging, the reaction products (i.e., poly-sodium sulfides) are transported through the surface of the glass fibers so as to provide enough space for further discharge reaction at the reaction front. The electrons and liquid sulfur are easily transported through the carbon fiber surface. The geometrical optimization of these glass and carbon fibers is important in order to characterize the overall cell performance.

2.5 The Electrical Insulating Header (IH)

Direct joining of the BASE to the remainder of the metallic cell is best avoided due to the large temperature fluctuations experienced during production, normal operation, and maintenance. Such temperature cycling is known to induce resultant thermomechanical induced stresses, due to the differences in CTE between the dissimilar material types incorporated in the cell [1]. Therefore, the inclusion of an alpha-alumina (α-alumina) insulating header (IH) between the electrolyte and surrounding metallic components has become common practice.

The α-alumina IH serves two essential purposes. First, it provides the required electrical insulation between the positively charged anode and negatively charged cathode containers throughout the life of the cell. Second, its presence offers increased strength and toughness for the fragile thin β-alumina electrolyte, at the point of attachment with the remainder of the surrounding metallic assembly. The material properties, primarily the differences in CTE values between the β-alumina electrolyte and α-alumina header, are therefore of extreme significance.

Typically, initial processing is performed to join the two ceramics, prior to mating the joined ceramic assembly to the remainder of the metallic cell components. To date, the bonding between the two ceramic components is conducted using a glass-sealing process. During this process, liquid glass is injected between the two ceramic components. This bonding, as well as the subsequently performed thermal compression bonding (TCB) technique, will be discussed in further detail as follows.

2.6 The Glass-Sealing (GS)

Externally induced thermal fluctuations during the manufacturing, normal operation, and the required maintenance intervals are a nuisance for the many dissimilar bonding locations within the cell. As stated, the hermetic glass-sealing bond is located at the BASE/α-alumina IH interface, while the TCB bonding process is conducted at the divisions separating the central ceramic segments of the cell with the outer metallic components.

Competent sealing between the thin walled BASE and α-alumina IH is of great importance for both safety precautions and maintaining the desired cell performance. Sealing between ceramic materials is difficult in practice due to the nature of the material

type itself. Of special concern are the inherent chemical inertness of ceramics, the low diffusion rates, and the relatively high melting temperatures [22].

2.6.1 Desired Properties of the Glass-Sealing

Glass-sealing materials have been commonplace in NaS cells for decades [1]. The advantages of using glass as the sealing material between the two ceramics include the chemical compatibility and similar CTE values. Additionally, the viscosity of the glass-sealing at temperatures well below the melting point of the ceramics makes the glass easy to manipulate without harming the previously sintered ceramics. Good wetting characteristics of the chosen glass-sealing also insure sufficient interface adherence [22]. Additional essential requirements of the glass include a complete hermetic seal, adequate resistance to both physical and thermal shock, and sufficient corrosion resistance against the molten reactants [23]. Many glasses can also be crystallized following the initial synthesis process, in order to improve upon both their mechanical and corrosion resistance properties [22].

Much work has been done to determine the influence of cell performance based upon variations in composition for the particular glass chosen. As stated, most of this research has revolved around maximizing the thermo-physical characteristics, including varying thermal expansion coefficients, glass transition (Tg) and softening (Ts) temperatures, along with changes in viscosities and densities [24].

2.6.2 Residual Stress Considerations

The final geometry of the glass-sealing material is somewhat variant based upon the construction techniques. Typically deposited at a temperature close to 950°C, the glass is in a liquid state, while the two adjacent ceramics retain their rigidity. Selection of the inherent CTE values as well as the ceramic geometries, plays an important role on the residual stresses left in the glass itself upon cooling. Ideally, a net radial compressive stress at room temperature is desired. However, at the operating temperature, the glass portion should be stress free [1]. This can be achieved by synthesizing the α-alumina IH with a slightly higher CTE value than the circumscribed β-alumina electrolyte wafer.

2.6.3 Thermal Shock Resistance

Thermal shock resistance at the ceramic glass interfaces is of particular importance to the work herein. As mentioned, differences in CTE values of neighboring components give rise to the possibility of premature or infantile failure. It is therefore important to closely match these characteristics between dissimilar materials, in an effort to avoid the initiation or propagation of micro cracks at the ceramic interfaces. Much research has focused on balancing the desired properties of the glass used at the ceramic-glass interfaces, although the more successful compositions remain mostly proprietary to date [22]. In addition to CTE equivalence, the pore or defect sizes at the glass interfaces, and the fracture toughness of the glass is also of great importance when attempting to prevent premature failures from occurring [23].

2.6.4 Glass-Sealing Materials

Most often, various alumino-borosilicate glasses are incorporated at the glass-sealing joints. These glasses are generally composed of SiO_2, Al_2O_3, and B_2O_3, along with alkali oxides including Li_2O, K_2O, Na_2O, MgO, among others present [1, 23-26]. Much successful work has also been conducted using bismuth-doped borosilicate glasses as well [24, 27]. In an effort to more closely match the CTE values of the adjacent ceramics with the glass, Shufeng, et al. [27] proved that bismuth doped borosilicate glasses, where the incorporation of Bi_2O_3 replaced varying concentrations of SiO_2, increased the CTE of the glass and decreased both the T_g and T_s temperatures of the resultant sealing glass.

For the present work, a glass with an inherent CTE value of approximately $6.9E^{-6}K^{-1}$ across the discussed temperature range was chosen in the standard model. A more through discussion of the cell component material properties will be fully addressed in Chapter 3.

2.7 Thermal Compression Bonding (TCB)

The other major joining technique mentioned previously within the NaS cell is employed at the metal-ceramic interfaces, and possess additional complications that must be taken into account. Thermal compression bonding (TCB), or diffusion bonding, is a process by which elevated temperature and pressures are applied in order to develop a localized diffusion-driven chemical bond. Performed at lower temperatures (~500 - 600°C) than the glass-sealing procedure (950°C), this process is subsequently employed to join the ceramic and glass assembly, to the surrounding metallic cell components.

Pioneered by Dawihl and Klinger (1969 [29]), Klomp (1971[30], 1972 [31]), and Harwell Laboratory by Nicholas and Crispin (1982 [32]), it was determined that the

incorporation of a soft metal interlayer (i.e. Al) between the ceramic and stainless steel case materials was advantageous. It was determined that the soft metal enables the accommodation of metal and ceramic components with substantially different CTE values to be successfully joined [1]. The work performed by Nicholas and Crispin [32] also discovered that when performed under vacuum, the resultant thickness of the intermetallic formed between the Al insert metal and stainless steel collars was maximized. Additionally, if post annealing was performed following the return to ambient pressures, the bond strength was further increased [32]. Further work carried out by Klomp (1971 [30]) showed that beyond a distance of 50 Å, no appreciable chemical reaction took place. Suggesting that the more common region for these seals to unintentionally separate is at the ceramic-Al interface. Provided that sufficient heating and pressure is induced to properly form the desired intermetallic bond between the Al and stainless steel.

The following (Chapter 3) will expand upon the already introduced material properties, as well as address the specific modeling techniques used during the present research. Explicit presentations of the geometry, mesh techniques, and boundary conditions will be provided. Discussion concerning the thermal profiles and any assumptions or simplifications used during the model development will also be addressed. Chapter 4 will then present the results of the many experimental computations, with appropriate thorough discussion provided.

Chapter 2 References Cited

15. J. L. Sudworth and A. R. Tilley, *The Sodium Sulphur Battery*, London: Chapman & Hall, pp. 5-255. 1985.

16. K. Jung, S. Lee, Y. C. Park, and C. S. Kim, Power Sources 250 (2014), pp. 1-14.

17. Z. Wen, Y. Hu, X. Wu, J. Han, and Z. Gu, Advanced Functioning. Materials, vol. 23, (2013), pp. 1005 – 1018.

18. D. H. Doughty, P. C. Butler, A. A. Akhil, N. H. Clark, and J. D. Boyes. The Electrochemical Society Interface Fall, (2010), pp. 49-53.

19. Chung, L. W., Ismail, A.B., Hussien, Z.F.. Proceedings for the National Power and Energy Conference, 2004. IEEE. 29-30 (Nov. 2004), pp. 205-210.

20. Ohi, J. M. Vol. I: Cell and Battery Safety, National Renewable Energy Laboratory. Sept. 1992.

21. Gupta, N. K. and Tischer, R. P. Electrochemical Society, Vol. 119, No. 8, (1972), pp. 1033-1037.

22. Weber, N. and Kummer, J. T. Proceedings form 21st Annual Power Sources Conference. (1967), pg. 37.

23. Rankin, G. A. and Merwin, H. E. Journal of American Chemical Society, Vol. 38, (1916), pg. 568.

24. Bragg, W. L., Gottfried, C. and West, J. Z. Kristallogr., Volume 77, (1933), pg. 255.

25. Tofield, B. C. *Intercalation Chemistry*, Academic Press, pg. 181. 1982.

26. Baffier, N., Badot, J. C. and Colomban, Ph., Materials Research Bulletin, Volume 16, (1981), pp. 259 - 265.

27. Boilot J. P. and Thery, J. Materials Research Bulletin, Volume 11, (1976), pg. 407.

28. Whittingham, M. S. and Huggins, R. A. The Journal of Chemical Physics 54, (1971), pg. 414.

29. Ormrod, S. E. and Kirk, D. L. Journal of Physics D.: Applied Physics, Vol. 10, (1977), pg. 1497.

30. Kim, K. K., Mundy, J. N. and Chen, W. K. Journal of Physics and Chemistry of Solids, Vol. 40, Issue 10, (1979), pp. 743- 755.

31. Sudworth, J. L., Hames, M. D., Storey, M. A., Azim, M. F. and Tilley, A. R. Journal of Power Sources, Volume 4, (ed. D. H. Collins), Oriel Press, (1973), pg. 1.

32. Bradhurst, D. H. and Buhanan, A. S. Australian Journal of Chemistry. (1961), pp. 397 – 409.

33. Gibson, A. Journal of Power Sources, Volume 6, (ed. D. H. Collins), Academic Press, London. (1977), pg. 673.

34. Hu, Y., Wen, Z., Wu, X., Lu, Y. Journal of Power Sources, Vol. 240, (2013), pp. 786-795.

35. Reed, D., Coffey, G. Journal of Power Sources, Vol. 227, (2013), pp. 94-100.

36. Shufeng Song, Zhaoyin Wen, Yu Liu, Xiangwei Wu, Jin Lin. Journal of Non-Crystalline Solids, Vol 357, (2011), pp. 3074 – 3079.

37. K. Jung, S. Lee, G. Kim, C. S. Kim. Journal of Power Sources, Vol. 269, (2014), pp. 773 – 782.

38. Shufeng Song, Zhaoyin Wen, Qunxi Zhang, Yu Liu. Journal of Power Sources, Vol. 195, (2010), pp. 384 – 388.

39. T.I. Barry, G.S. Schajer, F.M. Stakpool, Deutscher Verlag fuer Schweisstechnik Conference, West-Germany, 1980.

40. D.S. Park, M.W. Breiter, B.S. Dunn, L. Navias, U.S. Patent, 1982, 4,341,849.

41. S. Song, Z. Wen, Y. Liu, X. Wu, J. Lin. Journal of Non-Crystalline Solids, Vol. 357 (2011), pp. 3074 – 3079.

42. Atlas of Stress-Strain Curves, 2nd edition, ASM International, 2002.

43. W. Dawihl, E. Klinger, *Ber. Dtsch. Keram. Ges*, 1969, vol. 46, pg. 12.

44. J. T. Klomp, Ceramics Science, (1971), vol. 5, pg. 501.

45. J. T. Klomp, Bulletin of American Ceramics, (1972), vol. 51, pg. 683.

46. M. G Nicholas and R. M. Crispin, Journal of Materials Science, vol. 17, (1982), pg. 3347.

Chapter 3 – Computational Model Development

Proper model representations of the subject NaS assembly are of the utmost importance in terms of forming meaningful FEA conclusions. By partitioning the NaS assembly into smaller more manageable sections composed of the various materials used in the design phase, one can obtain a more accurate representation of the real world assembly. This chapter will begin by introducing the prototype planar-type cell chosen for the computational work herein, and continue by documenting the various FEA simulation methods chosen to complete the various experimental trials. In this Chapter, the geometry of the subject NaS cell and mesh generation tactics will first be described, followed by an introduction to the material properties of the various components incorporated in the cell. Next the computational methods used during the experimental trials will be addressed. In particular, the thermal loading and boundary conditions used during the simulation process are formally documented and explained. The common issues and assumptions or simplifications used in the subject work will also be addressed here.

3.1 Model Generation

3.1.1 Geometric Considerations

Meaningful computational analysis of the subject NaS cell begins by generating a realistic solid model representation of each of the individually joined components. As stated, the closer the model is to the real world design, the more accurate the anticipated results

will be. Therefore, it is crucial that the intricacies of each element are properly portrayed in the final model, and the interactions between neighboring members be accurately represented.

In the present work, the planar-type NaS cell model was digitized using a commercial software by the name of Rhinoceros® 5.0 (Robert McNeel & Associates, Indianapolis, IN, USA). Once drafted, the meshing of each component was then completed using Hypermesh 11.0 software (Altair Engineering, Inc., USA). Initial assembly investigations conducted by the Research Institute of Industrial Science & Technology (RIST, South Korea) group indicated the most successful dimensions of the various components during prototyping.

The resultant meshed components were then rotated around a centrally located cylindrical quadrate axis, in an effort to create a model similar to that shown in Figure 3.1. The substantially different aspect ratios for the parts is evident. The differing aspect ratios place a significant burden during the model development phase, as care must be given when choosing the element types and numbers to be incorporated. The meshed parts were then transferred into a finite element software package called ABAQUS FEA 6.11-2 (Dassault Systemes) for creation and completion of the experimental thermal loading profiles, as well as obtaining and interpreting the results of the various trials (pre-processing, processing, and post-processing).

As shown, the cross-sectional view of the prototype cell used in this work exhibits the many individual components described in the previous cell background chapter. Due to the complexity of the cell in this area, the central insulating header region is shown in the expanded portion of Figure 3.1. This area of the cell is of high concern because of the multitude of differing CTE values of the joined components, which makes this region

particularly susceptible to high stress accumulation, in conjunction with the resultant severe elastic/plastic deformations that are known to cause failure [1].

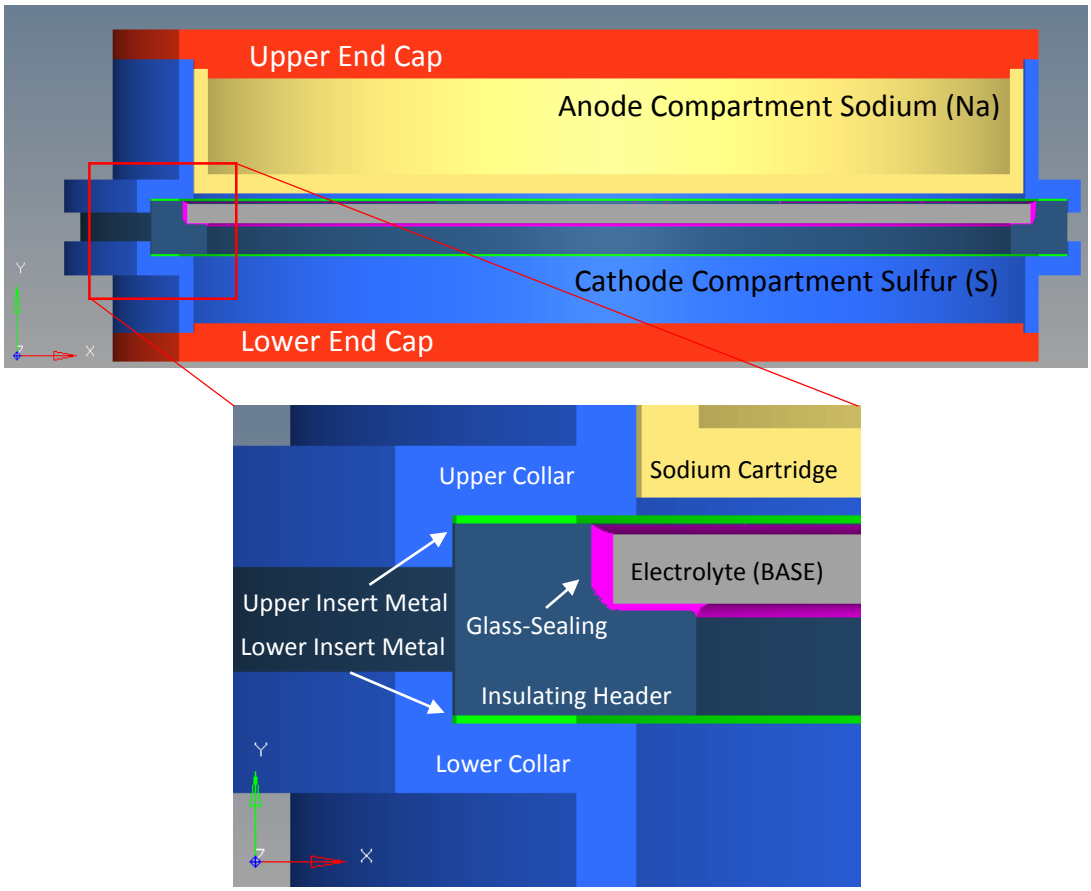

Fig. 3.1-A cross section of the prototype cell geometry used in the current research. A localized view (lower) of the model used for the subject analysis clearly depicts the α-alumina header (central - dark blue) and β-alumina electrolyte (gray), with the glass sealant (purple) between them. The insert metals (green), cartridge (yellow), and collars (bright blue) are also shown.

The resultant induced thermomechanical stresses are also known to increase, as the overall diameter of the cell is increased. To date, much success has been encountered when developing cells with electrolyte disks below 100 mm in diameter; however, cells with 120mm diameters and larger exhibit excessively high failure rates during synthesis. Therefore, the exploration of a 120mm electrolyte disc cell was chosen as the focus of this work.

As described, the α–alumina IH itself and the β-alumina electrolyte are joined by the incorporation of a glass sealant, and the joined ceramic assembly is then attached to the remainder of the stainless steel metallic container. These previously described TCB joining sites pose significant challenges during the assembly process, and failure is often encountered in two forms. Interfacial separation at the ceramic/insert metal, and bulk failure through the ceramics are of particular concern [1]. Therefore, care must be taken in order to properly represent these components within the representative model. Generally speaking, an increase in the number of mesh elements in the region's most likely to encounter excessive or unpredictable loading or interactions is common practice [2, 3].

It should be noted that some of the aforementioned components of the cell such as the cathode carbon/glass fiber felt and the reactants themselves were ignored in the computation because their effect on the resultant thermomechanical stresses at the thermal compression bonding sites and adjacent cell components are negligible [1].

3.1.2 Mesh Generation

In the finalized planar-cell model, used in the majority of the trials, a total number of 448,621 mesh elements were chosen for the representative 30-degree slice (axis-symmetric model) shown in Figure 3.2 (standard control model). The figure depicts each of the FEA

meshes developed for the various components in the same scale, clearly illustrating the similar, but differing mesh sizes strategically chosen for each.

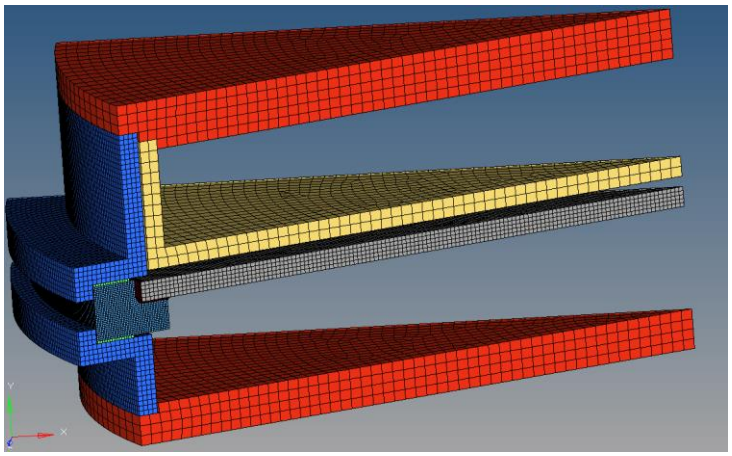

Fig. 3.2-Meshed 30° degree slice of the model (axis-symmetric model) developed for the majority of the subject study. The components near the insulating header region were intentionally reduced in size to more accurately investigate the resultant induced thermal loading influences.

As stated, setting a proper mesh quality is a critical step in accurately representing the actual cell components and obtaining the intended high degree of accuracy. Several criteria for evaluating the quality of the developed mesh are available within the Hypermesh software package. The aspect ratio of each component is of particular concern, and it is highly recommended that this ratio should be maintained below 5.0 for each meshed object in the assembly. For the present work, the aspect ratio for all of the cell components was kept below 4.0, in an effort to more to accurately portray the representative components of the cell. Jacobian and skew characteristics of the mesh are additional characteristics that indicate the quality of the developed mesh, and were also routinely taken into account during the digitization process.

The total number of elements was empirically determined, keeping in mind the balance between the computational assets associated with the miniaturization of the elements and the maintained accuracy of the intended results. That being said, the computational time required for many of the models over the temperature cycles proposed, took several days to complete using parallelized computing schemes utilizing 32 CPUs with 128GB of memory. The total number of mesh elements chosen for each component in the assembly is summarized in Table 3.1.

Table 3.1-Summary of the number of mesh elements and material types used for each of the subject cell components for the majority of the trials (unless otherwise noted).

Component	No. of Mesh Elements	Material Type
Insulating Header	301,045	α-alumina
Glass-sealant	94,955	Glass
Electrolyte	23,555	β-alumina
Upper Collar	10,560	STS-431
Lower Collar	7,440	STS-431
Cartridge	1,616	STS-431
Upper Insert Metal	1,800	Al-3003
Lower Insert Metal	1,800	Al-3003
Upper Cap	3,222	STS-431
Lower Cap	2,628	STS-431
Total	**448,621**	**--**

In the subject model, the basic mesh type chosen was an 8-node linear brick (C3D8R); reduced integration mesh element. Hexahedron meshes are essentially made up of 3D topological cubes with 8 vertices and 12 edges, which are bound by 6 quadrilateral faces [4, 5]. Inherent benefits of these particular types of mesh elements versus the many other types available, include generally improved accuracy, higher resolution, ease of convergence, and the ability to easily vary the elemental size without fear of inducing false or unintended

surface or bulk defects [4, 5]. This 3D type solid element also has the advantage of evaluating the accumulated stress through the thickness of the various components; however, it does require an accompanying need for increased computational resources.

3.2 Material Properties

As mentioned, the subject planar-type NaS cells are composed of many different dissimilar material types including metals such as stainless steels (STS) and aluminum (Al) alloys; α- and β'/β"-alumina ceramics, glass, and carbon. It is essential to be as accurate as possible when specifying the temperature dependent thermomechanical properties of each material type, in an effort to accurately portray the intersections between the components they comprise. Within the ABAQUS software, material properties such as the elastic modulus, Poisson's ratio, and stress-strain data are imported by the user for each material. This data is essential for proper representation. The incorporation of both STS and Al alloys (STS431 and Al3003, respectively) are widely implemented for structural components of many modern NaS cells. These materials inherent low cost, desired machinability and/or formability, as well as sufficient surface wettability, and high corrosion resistance make them ideal candidates [1].

The relevant physical and mechanical properties of the materials included within the subject NaS model are summarized in Table 3.2. As stated, temperature dependence for both modulus and CTE variation were taken into account as well, and those curves are shown in Figure 3.3. Additionally the temperature dependent stress strain curves for both Al3003 and STS431 are shown in Figure 3.4.

Table 3.2 - Summary of physical and thermomechanical properties of materials in the header area of the subject planar NaS battery assembly (Data was measured during the prototype phase (glass) or obtained from ASM International [6]).

Material Type	Modulus of Elasticity	Poisson's Ratio	Coefficient of Thermal Expansion
Al3003	Temperature Dependent See Fig. 3.3a	0.33	Temperature Dependent See Fig. 3.3b
STS431		0.28	
α-alumina		0.23	
β-alumina		0.23	
Glass	62 GPa	0.22	6.9 x 10^{-6}/K

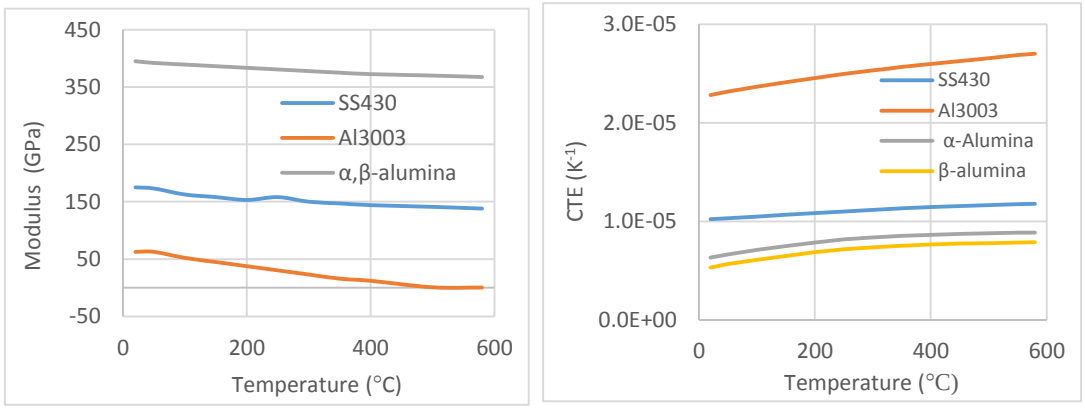

(a) **(b)**

Fig. 3.3-Curves obtained for the elastic modulus **(a)** and CTE values **(b)** across the temperature range of 20 - 580°C for each material type [6].

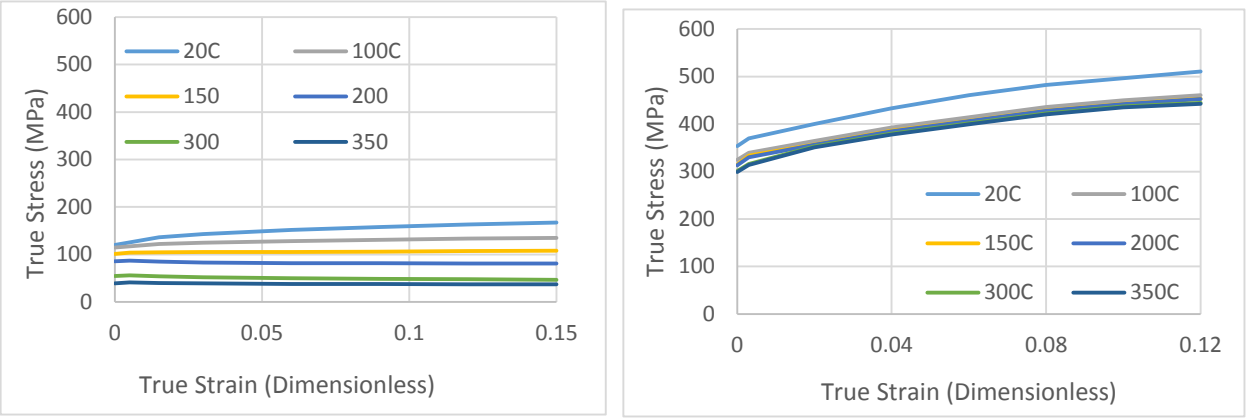

(a) **(b)**

Fig. 3.4-The stress-strain curves obtained for Al3003 **(a)** and stainless steel 431 **(b)** across the subject temperature range of 20 - 350°C [6].

3.2.1 Stainless Steels

The faultless containment of the high temperature volatile reactants has forced developers to adopt chromium-rich STS alloys for the reactant containers [1, 7]. The desired mechanical properties and general high strength and toughness of stainless steels make them an obvious choice for exterior surfaces as well. The combination of these benefits, paired with the inherent CTE values near those of the ceramics contained within, make them the clear choice for the majority of the metallic cell components. In the present study, STS alloy UNS S43100 (AISI 431, STS431) was selected, based on the conjunctive prototype work being done by RIST. In addition to an elevated chromium contact (15.0 – 17.0 wt. %), this martensitic stainless alloy exhibits a somewhat elevated nickel content (1.25 – 2.50 wt. %) when compared with other ferritic or martensitic grades [8].

3.2.2 Aluminum Alloys

Aluminum alloys as construction materials have also been investigated in the planar type NaS cells. These alloys are typically easier to fabricate than stainless steel options, but lack the strength and overall durability that steel alloys exhibit. As evidenced in Figure 3.3b, the CTE mismatches are much more significant between most Al alloys and the enclosed ceramic components of the cell, when compared to those of the designated STS431 alloy. The increased variance in CTE values will of course contribute to higher induced stresses in the ceramic components upon thermal loading.

As touched upon earlier, Al alloys are however beneficially incorporated into most planar-type NaS cells at the thermal compression bonding sites. The Al alloy chosen for the subject analysis is UNS A93003 (AISI 3003, Al3003). This alloy exhibits good machinability, decent strength, superior weldability, good corrosion resistance, and an annealing temperature of about 413°C (above typical cell operation temperatures). The low modulus of elasticity of this material allows for stress absorption in the Al 3003, and this inherent absorption was noted as significantly reducing the resultant stress concentrations in the glass-sealing and other components by K. Jung et al. [9].

3.3 Computational Conditions

3.3.1 Coordinate System Set-up

By default the more intuitive Cartesian coordinate system is the default system within the ABAQUS/Standard workspace. The cylindrical nature of the planar-type NaS cell geometry, however, more easily lends itself to the incorporation of a cylindrical system. A

cylindrical coordinate system allows for easier analysis in both the longitudinal, circumferential, and radial directions. The relationship between the two systems is shown for visual clarity in Figure 3.5.

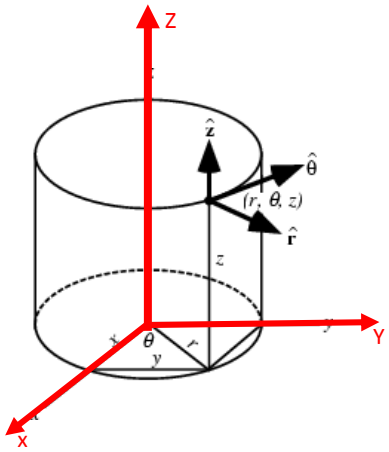

Fig. 3.5-Relationship between the Cartesian coordinate system (red) and associated cylindrical system (black) [10].

As the figure suggests, the x, y, and z directions in the Cartesian coordinate system are represented as r (radial), θ (circumferential), and z (vertical) directions in the cylindrical system respectfully. The Implemented global cylindrical system chosen during the model development stage for the standard planar-type cell is shown in Figure 3.6.

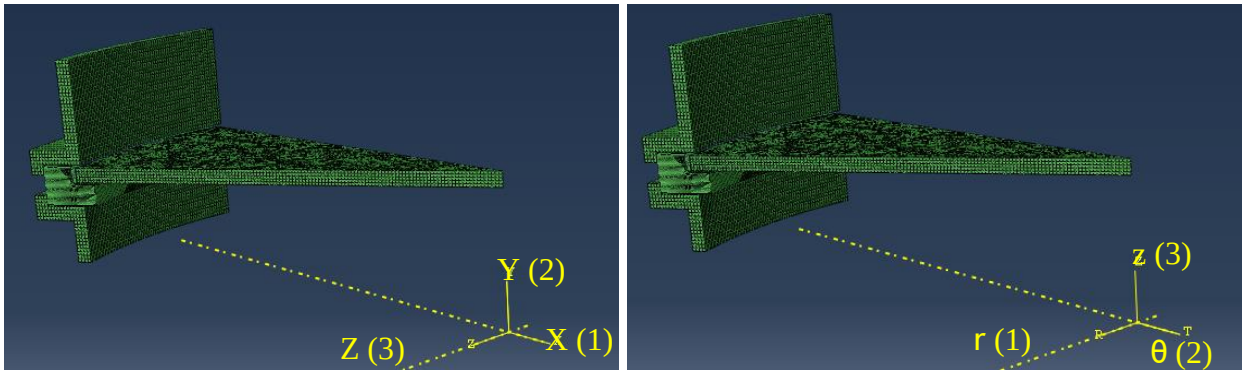

(a) **(b)**

Fig. 3.6-The global Cartesian **(a)** and cylindrical **(b)** coordinate systems designated for the majority of the trials are shown for the standard 30° slice model.

As the figure indicates for the cylindrical system, the radial (r), circumferential (θ), and vertical z-axis were chosen as shown. This means that in the cylindrical system the vertical measured normal stresses for the surfaces in the cell were measured in the σ_{33} (vertical) direction, while the shear stresses on horizontal surfaces within the cell were measured in the τ_{13} direction. Due to the overall radial shrinkage of the outer metallic container during cooling, the normal stresses in the electrolyte were measured in the σ_{11} direction in the cylindrical system.

The coordinate system used to determine the maximum normal stress of the glass-sealing is local position-dependent. In other words, the normal stress in the glass-sealing were determined on the inner-most curved surface, and therefore, measurements were not possible using either the global Cartesian or subsequently established cylindrical system. These stresses could only be accurately determined by establishing a localized rectangular coordinate system. The established localized coordinate system implemented for the curved

glass-sealing surface is shown in Figure 3.7. In this coordinate system, the normal stress measured is therefore in the σ_{22} direction (y-direction).

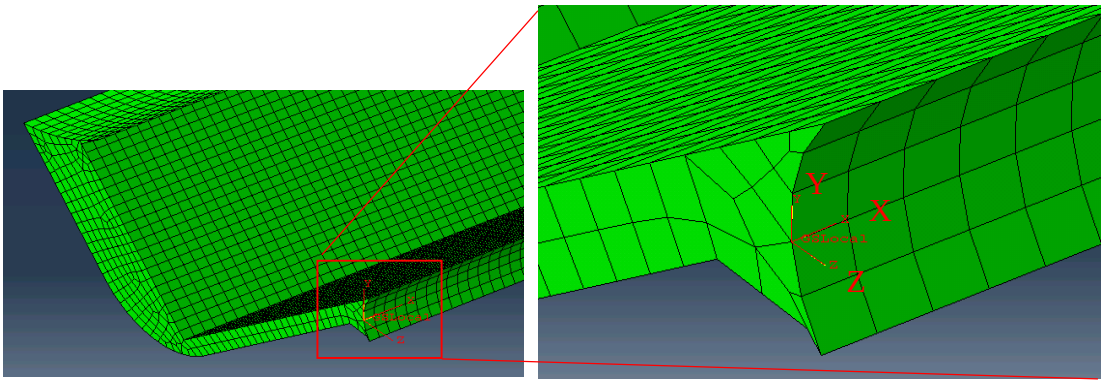

Fig. 3.7-The localized rectangular coordinate system established to obtain the normal stresses calculated on the inner-most glass-sealing curved surface.

3.3.2 Experimental Trials Defined

The thermally induced stresses in the planar-type NaS cell are a direct result of the mismatches in the CTE values of the various materials within. Therefore, the logical way in which to reduce the resultant stresses is to more closely match the CTE values of the neighboring components. After running a standard or control cell, trials documenting changes in the CTE for both the glass-sealing and stainless steel container materials were implemented. Geometry of the individual cell components also greatly influences the resultant stresses. To investigate this, the thicknesses of the Al inset metals were modified, as well as the thicknesses of the cell container materials. Additionally, due to the high fallout rate of the β-alumina electrolyte during prototyping, an effort was made to determine the effects of a misaligned, or off-center electrolyte disk in the glass-sealing, was also investigated. All of the specific modifications made to the various material CTE's, while

holding the temperature profile constant (see Figure 3.8), are shown in the experimental decision matrix (Table 3.3) which follows.

Table 3.3-Experimental matrix showing the various cell modifications that were implemented during the computational trials.

Trial	Description of the Computational Trials	Induced Computational Variables
1	Control	No CTE variance, all standard material properties employed
2	Glass-Sealing, CTE Variance	Glass-Sealing CTE values of $5.0E^{-6}$, $6.0E^{-6}$, $6.9E^{-6}$ (control), & $8.0E^{-6}$-K
3	Stainless Steel, CTE Variance	Average STS CTE values of $1.11E^{-5}$ (control) , $10.01E^{-5}$ and $9.11E^{-5}$-K (See Fig. 4.15)
4	Aluminum Thickness Variance	0.1875mm, 0.25mm (control), & 0.3125mm
5	Stainless Steel Container Thickness Variance	1.5mm, 2mm (control), & 2.5mm
6	Potential Electrolyte Disk Centering Issues	50 % Transverse Shift, (See Fig. 4.28)

3.3.3 Thermal Loading Considerations

Knowledge of the various processes involved during the synthesis of the cell is crucial in accurately depicting the thermal loading conditions that are induced. As eluted earlier, two main joining techniques are implemented, and the temperatures required for these processes must be taken into consideration when modeling the representative cell. The glass-sealing operation joining the ceramic insulating header to the essential electrolyte component takes place at 950°C, while the subsequent TCB joining process is carried out at 520°C. Before and after each of these temperature increases, the model is assumed at room temperature (20°C).

Assuming the glass softening (T_s) also occurs near 520°C, the resultant simulations were subdivided into three steps that were carried out for the majority of the experimental trials. It should also be noted that the glass-sealing step was truncated due to the materials inherent elastic behavior, allowing for the simulation to begin at the T_s temperature of ~520°C. This is also the temperature where the subsequent TCB bonding is performed to join the ceramic components to the neighboring STS case material. The temperature cycling is shown schematically in Figure 3.8. An initial glass-sealing step was conducted, followed by the "thaw-freeze" cycles shown.

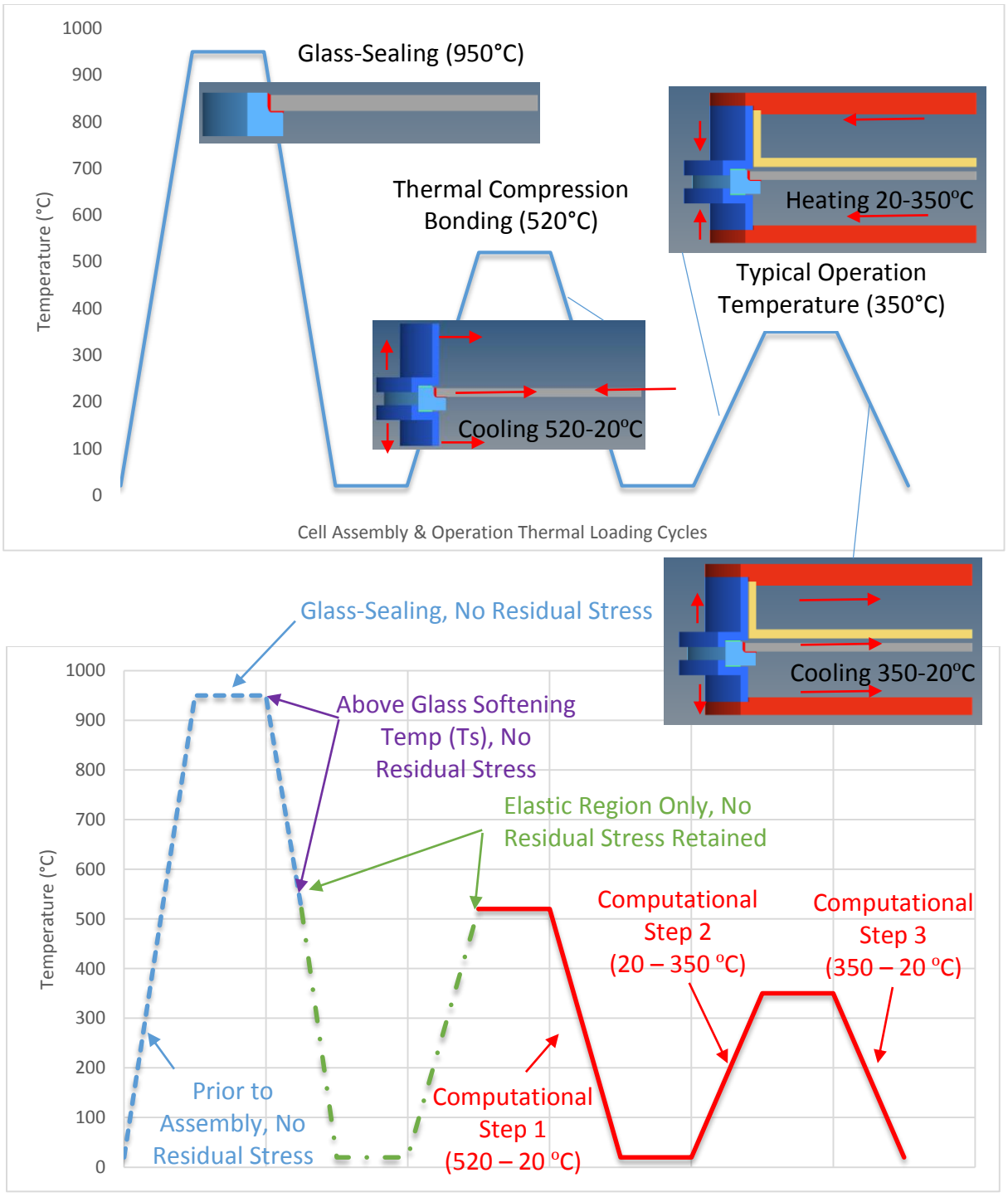

Fig. 3.8-Thermal loading profiles based upon the cell construction sequence. The construction sequence and induced thermomechanical loading directions are shown (upper). The temperature cycles used for the majority of the simulations conducted in the subject trials is shown in red (lower).

3.3.4 Boundary and Loading Conditions

To more accurately depict the actual model deformations during thermal cycling, the boundary and loading conditions of the representative FEA model must reflect the actual conditions imposed. In the subject NaS cell, the diameter of the cell should be allowed to freely expand and contract along the radial and longitudinal directions. Rigid body motion must however be prevented, and is induced by the incorporation of constraints imposed on the lower nodal plane of the cell. These elements are therefore constrained from displacement in the longitudinal direction. This prevents any unintended rotational or translational movement from occurring based upon the resultant thermal expansion or contractions encountered during the heating and cooling cycles. The specific surfaces chosen to implement the vertical displacement boundary condition for both the step 1, and steps 2 & 3, models are shown in Figure 3.9.

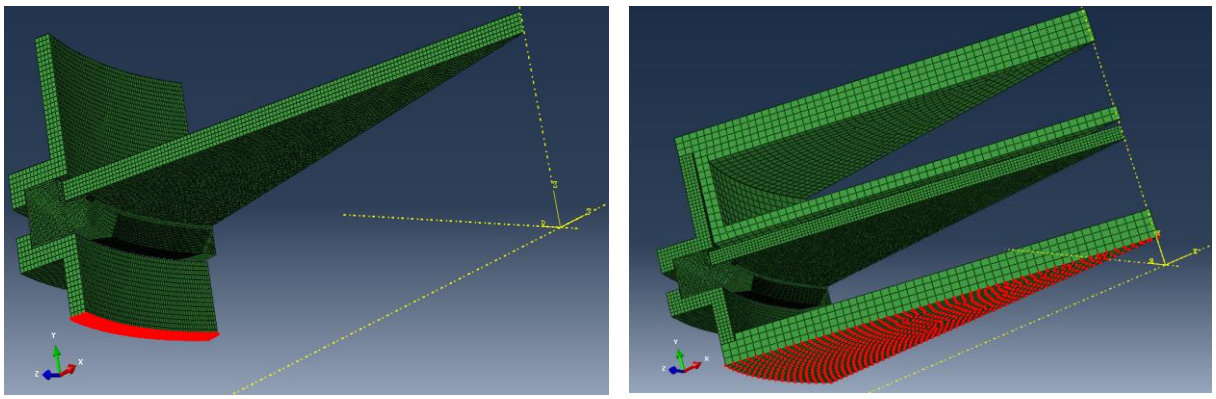

Fig. 3.9-Vertical displacement boundary condition imposed on both the step 1 (left) and steps 2 and 3 (right).

Symmetric boundary conditions (i.e., axis-symmetric model) were also imposed in an effort to reduce the computational resources required for each of the individual simulations. Incorporation of the symmetric boundary conditions requires the nodes along the symmetric plane (vertical direction in the subject models) to have zero displacement in the direction normal to the symmetric plane (circumferential). This was achieved by holding zero-displacement in the YSYMM (UR2=UR1=UR3=0) direction in the ABAQUS software package. The surfaces chosen for both the step 1 and steps 2 and 3 models are shown in Figure 3.10.

Assigning the proper interfacial conditions between the various components of the representative model is also of paramount importance. In the present work, a non-sliding, high friction (tie-condition) was assumed at all component interfaces.

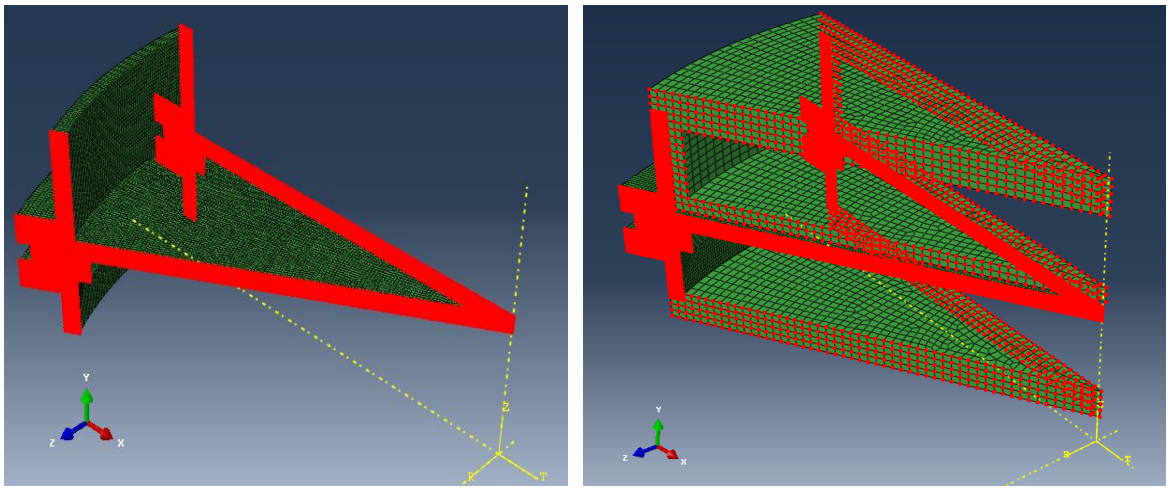

Fig. 3.10-Symmetric boundary condition imposed on both the step 1 (left) and steps 2 and 3 (right).

3.4 Strategic Assumptions and Simplifications

Throughout the simulations carried out in the present work, thermally static computations were assumed. Although it is known that both endothermic and exothermic electrochemical reactions are contained within the electrode compartments during the charge and discharge cycles, these effects were hypothesized as negligible, due to the slow heating and cooling cycles implemented during booting and shut-down (30-50 hours, slower than 0.5°C min-1 [1]). These slow heating and cooling cycles are exercised in an effort to prevent thermal shock and resultant premature failure, which could potentially develop due to the CTE mismatches addressed previously.

Additionally, internal temperature gradients through the bulk of the component thicknesses were also intentionally disregarded. The header location is held at ~550°C for relatively long periods of time during the TCB bonding operation, so the Al can be considered in the annealed condition, free from appreciable internal residual stresses. Therefore, these residual stresses were not taken into consideration. Effects of the carbon felt within the cathode compartment were also neglected [1].

Although slow heating and cooling cycles are implemented during the thaw-freeze cycles, continued temperature cycling for maintenance or other unforeseen reasons during the service life of the cell can lead to plastically accumulated residual stresses in the susceptible members of the cell. As was documented, only an initial thaw-freeze cycle was implemented, leaving the door open to further work in the future.

Chapter 3 References Cited

1. K. Jung, S. Lee, G. Kim, Y. C. Park, C. S. Kim. Journal of Power Sources, Vol. 250, (2014), pp. 1 – 14.

2. B. Wah, The Finite Element Method. Wiley Encyclopedia of Computer Science and Engineering. John Wiley & Sons, Inc. (2008).

3. P. Widas. Virginia Tech Material Science and Engineering. (1997).

4. Unknown, Department of Aerospace Engineering Sciences, University of Colorado at Boulder. 2013.

5. J. E. Castillo, Society for Industrial and applied Mathematics, Philadelphia. 1991.

6. ASM International, *Atlas of Stress-Strain Curves*, 2nd Ed. 2002.

7. J. L. Sudworth and A. R. Tilley, *The Sodium Sulphur Battery*, London: Chapman & Hall, 1985.

8. ASTM Standard A276-15, "Standard Specification for Stainless Steel Bars & Shapes," ASTM International, West Conshohocken, PA, 2015.

9. K. Jung, S. Lee, G. Kim, C. S. Kim. Journal of Power Sources, Vol. 269, (2014), pp. 773 – 782.

10. E. W. Weisstein, Michigan State University. http://archive.lib.msu.edu/crcmath/math/math/c/c909.htm

Chapter 4 – Computational Results & Formal Discussion

This chapter will address the FEA computational results obtained during the various computations conducted using the planar-type NaS cell. A full discussion of the thermally induced stresses within the construction materials will be addressed, with particular emphasis on the interfaces between dissimilar materials, and the bulk stresses within the brittle ceramic and glass components of the cell. The stresses investigated were determined as localized maxima in the normal and shear directions on the component surfaces, and the impact of these elevated values will be weighed. As mentioned previously, a full treatment of the standard planar-type cell will be completed, followed by the addition of the five main adaptations; these include variances in the CTE values for the glass-sealing and STS 431 container materials. Other modifications include the thicknesses of the aluminum insert metals and stainless steel container collars, as well as the aforementioned electrolyte centering concerns. A full treatment of the stresses found in the major components will be thoroughly explored with visual aids summarizing where these stresses were obtained.

4.1 Standard Planar-Type Cell Computations

This section addresses the various accumulated stresses in the individual components where the maximum localized values were identified in both the normal and shear directions of the standard cell. Separated by the individual cell components, the localized maximum stresses and their inherent ramifications will be discussed.

4.1.1 α-Alumina Electrical Insulating Header

The four maximum localized normal stresses measured in the σ33 (vertical, cell height direction) direction at various surfaces of the insulating header were first analyzed for the standard cell configuration. The specific surfaces where the normal stresses were obtained are illustrated following the initial cool step (520 - 20ºC) in Figure 4.1a. In addition to the normal stresses at the upper and lower insert metal interfaces (red circles), the maximum stress values were also obtained at the outer and innermost vertical surfaces of the header, near the top (yellow circles). The highest measured normal stress identified was present near the top of the outer normal vertical surface (left), where a value of approximately 270 MPa was identified.

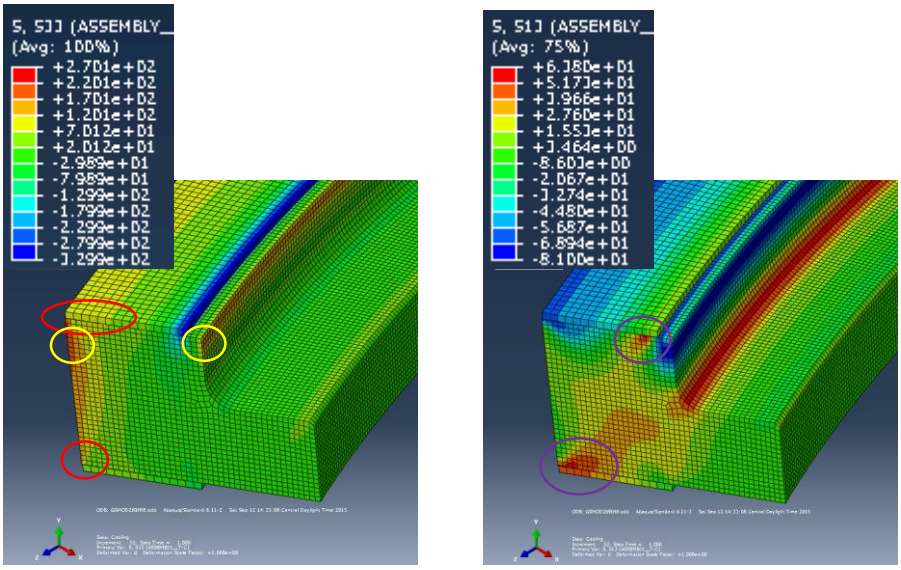

(a) **(b)**

Fig. 4.1-Stress distributions in α-alumina electrical insulating header indicating the areas of maximum measured stresses in both the **(a)** normal and **(b)** shear directions of the standard cell. The adjacent upper and lower insert metals are also shown for reference (upper & lower surfaces).

The maximum shear stress values in the τ_{13} direction were also measured at the upper and lower horizontal surfaces, as shown in Figure 4.1b (purple circles). As documented in Table 4.1, the maximum shear stress at the upper surface was found after the final cooling step (350 - 20°C), while the maximum at the lower surface was obtained following the initial (520- 20°C) cooling cycle.

As the table indicates, the thermomechanical induced stresses in both normal and shear directions were similar, however, greater at the upper insert metal interface, than at the lower inset metal interface. In relation to the vertical surfaces of the header, these values were significantly less, and the maximum stress, as stated previously, was near the top of the outer most vertical surface. The positive stress values are associated with localized tensile stresses in the brittle α-alumina insulating header. Ceramic materials are inherently brittle and resist all elastic deformation, and therefore, the high measured tensile stress concentrations near the top of the outer vertical surface, is an indication of the most likely region of potential thermomechanical failure.

Table 4.1-Calculated localized normal and shear stress values obtained from the outer, inner, and upper surfaces of the electrical insulating header in the standard planar-type cell following each of the three induced temperature cycles.

Stress Location	Measured Stress (MPa)		
	Step 1 520 – 20°C	Step 2 20 – 350°C	Step 3 350 – 20°C
IH Outer Normal	269.99	-1714.70	178.48
IH Inner Normal	129.23	-1854.31	86.26
IH Upper Normal	88.56	-1888.55	23.68
IH Upper Shear	63.53	60.06	64.43
IH Lower Normal	70.83	-1898.71	-44.08
IH Lower Shear	61.02	58.04	58.26

*: Negative Values indicate compressive stresses

Graphical representations of the six localized maximum stresses identified on the surfaces of the insulating header, as a function of the induced temperature cycling are shown in Figure 4.2. This data was obtained from the FEA element that exhibited the maximum stress values.

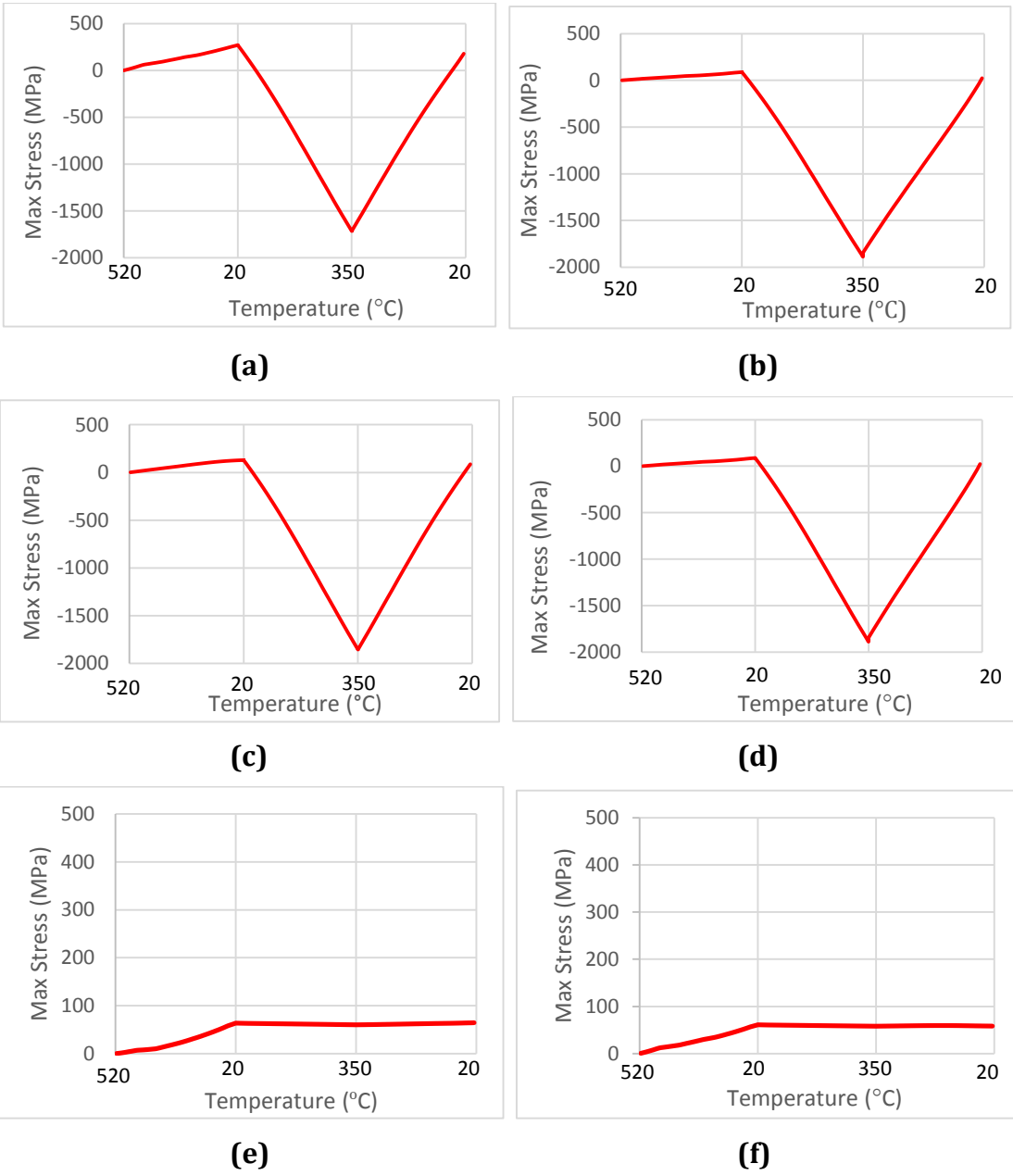

Fig. 4.2-Maximum localized normal and shear stress plots using the three step temperature ramping outlined in Figure 3.8. **(a)** outer normal, **(b)** upper normal; **(c)** inner normal; **(d)** lower normal, **(e)** upper shear, and **(f)** lower shear.

Although the values vary between the specific locations, the general trends for each of the normal and shear directions are similar to one another. In the normal direction plots **(a-d)**, a gradual positive slope is present during the initial temperature cycle, followed by a much more dramatic negative slope upon heating. Finally, a much greater positive slope upon the final cooling step is evident. This general trend is based upon the construction sequence of the cell, as addressed in Chapter 3. Figure 4.3 (Fig. 3.8a reproduced) previously defined the construction parameters as they relate to the chosen temperature profiles used for the subject investigations.

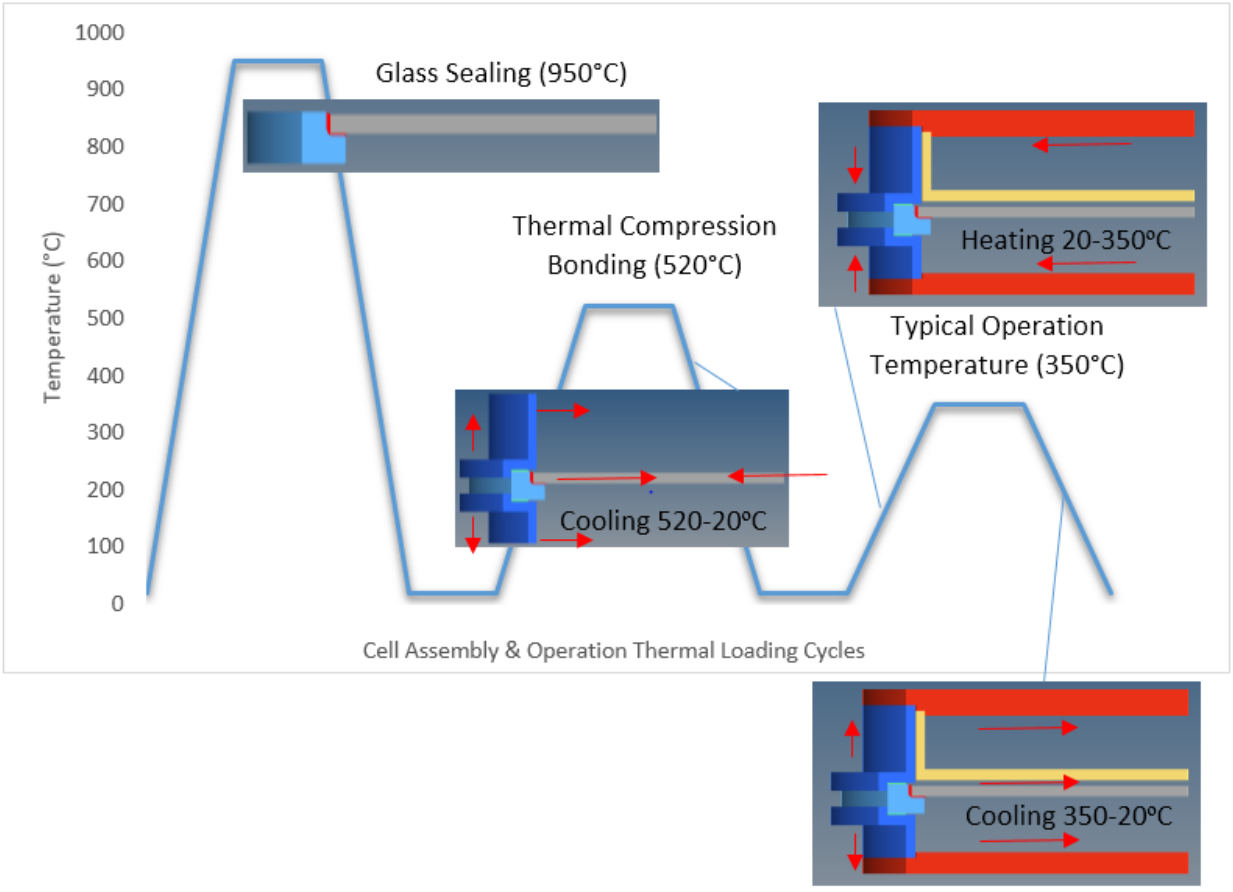

Fig. 4.3-Reproduction of Figure3.8a, to more clearly define the resultant graphical trends shown in Figure 4.2, and replicated in additional cell components to follow.

Thermal compression bonding (TCB) to attach the upper and lower container collars to the central ceramic assembly is conducted at 520°, where our simulation begins. Immediately following the TCB process, cooling to 20°C causes the diameter of the outer container to contract in the radial direction, initiating the resultant normal tensile stresses in the centrally located ceramic components (initial positive slope). Upon subsequent heating, following joining of the upper and lower caps and cartridge to the cell, both the container and caps expand radially, inducing the resultant compressive stresses in the normal direction (negative slope). Subsequent cooling from 350 to 20°C, then again induces a more dramatic radial contraction of the cell, inducing the final tensile stresses in the central ceramic assembly (greater positive slope).

4.1.2 Upper and Lower Insert Metals

The thermal compression bonded Al3003 alloy insert metals are located at the interfaces between the α-alumina electrical insulating header and adjacent STS431 structural collars. Normal and shear stresses were obtained from both the upper and lower surfaces of each insert. It was determined that the maximum normal stress concentrations were higher towards the outside edge of the upper insert, and the shear stress concentrations were greatest at the outer edge of the lower insert. The differences in measured stresses between the upper and lower surfaces of each insert were negligible, and therefore although similar, the reported values were chosen at the relevant interface surfaces.

Similar to the insulating header results reported prior, the localized normal and shear stress concentration locations are shown in Figure 4.4. The measured values following each

computational steps are summarized in Table 4.2, and the plots obtained are outlined in Figure 4.5. In the figures, IM1 refers to the upper and IM2 the lower insert metals, respectively.

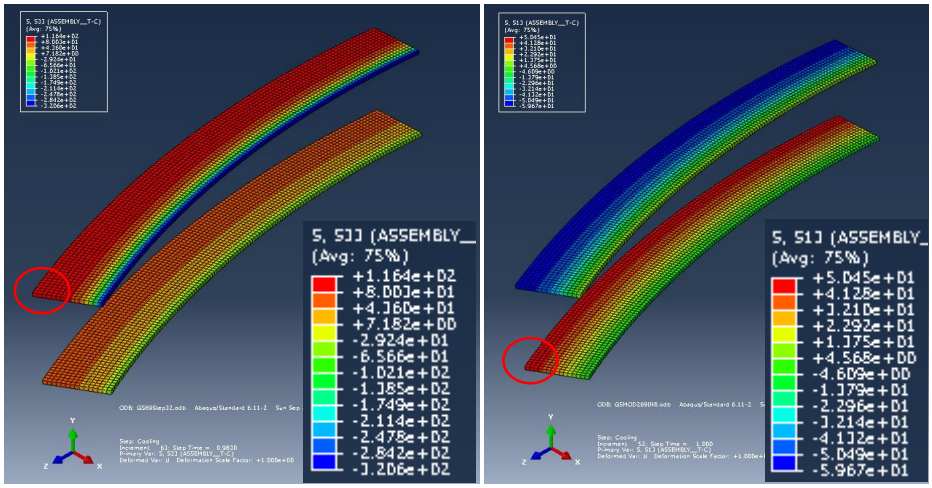

(a) **(b)**

Fig. 4.4-Stress distributions in the upper and lower insert metals indicating the areas of maximum localized stresses (red circles) in both the **(a)** normal and **(b)** shear directions.

Table 4.2-Calculated localized normal and shear stress values obtained from the upper and lower insert metals in the standard planar-type cell following each of the three temperature cycles.

Component	Stress Location	Measured Stress (MPa)		
		Step 1 520 – 20°C	Step 2 20 – 350°C	Step 3 350 – 20°C
Upper Insert Metal 1	Upper Normal	80.54	-373.19	116.42
	Lower Normal	80.52	-374.95	116.43
	Upper Shear	11.33	2.53	11.86
	Lower Shear	11.28	2.51	11.76
Lower Insert Metal 2	Upper Normal	34.62	-384.60	74.15
	Lower Normal	34.62	-384.62	74.14
	Upper Shear	50.45	11.21	48.84
	Lower Shear	50.40	11.23	48.81

*: Negative values indicate compressive stresses

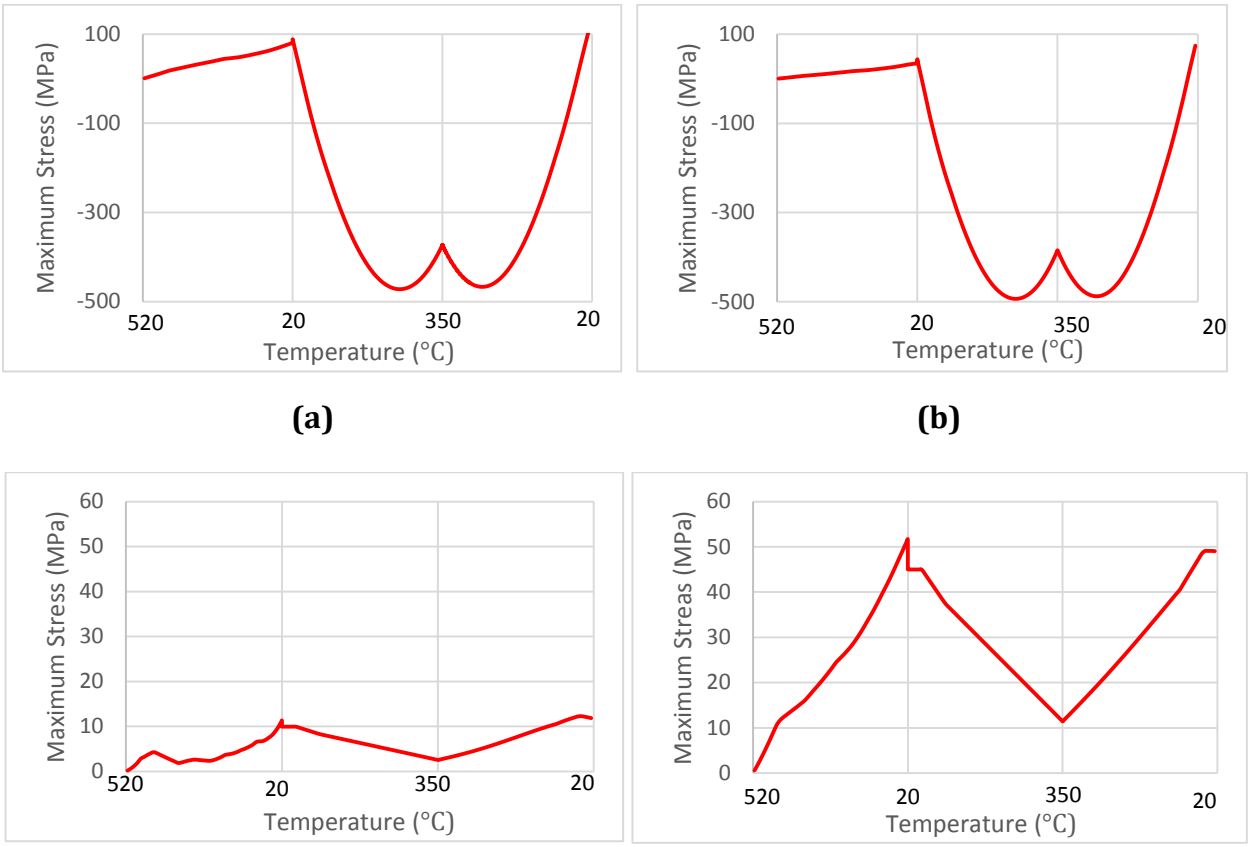

Fig. 4.5-Maximum localized upper and lower insert metal normal and shear stress plots using the three step temperature cycles outlined in Figure 4.3. **(a)** IM1 lower normal, **(b)** IM2 upper normal, **(c)** IM1 lower shear, and **(d)** IM2 Upper shear.

As shown, the maximum shear stress for all but the lower insert metal were highest following the final cooling cycle from 350 – 20°C. Although close in magnitude, the upper and lower shear for the lower insert metal was a maximum following the initial cooling from 520 - 20°C. The same general trend based upon the construction sequence was experienced by the insert metals, as was found in the insulating header in regards to the normal stress plots (Fig, 4.5 a-b).

There is a distinct difference near the cell operation temperature of 350°C however. Instead of a maximum compressive stress as was witnessed in the insulating header, a slight decrease of approximately 100 MPa in the normal (compressive) stress is evident. This decrease seems to begin at approximately 275°C, which is associated with a stress relaxation temperature of the chosen Al3003 alloy [1]. In other words, the modulus values and the stress values (in the strain-strain curve) of Al3003 are substantially decreased in this temperature range, which gives rises to a relative increase in the stress profile compared with the one in the lower temperature. Although the annealing temperature isn't reached until approximately 413°C, some plastic deformation will be evident well before that temperature is reached, and is what accounts for the "W" shape of the plots in Figure 4.5a&b.

Though the general shape is similar, the obtained shear values are much lower in the upper inset than those in the lower insert metal. This indicates a larger radial sliding stress at the lower insert than at the upper. This is likely a function of the cell configuration differences near the two inserts. The proximity of the centrally located ridged glass-sealing and electrolyte are closer to the upper insert than the lower. Thus, less radial deformation is possible near the upper insert, accounting for the lower measured shear stress values at the upper insert interfaces. The general trend of the two shear plots is similar, and is again related to the construction sequence documented in Figure 4.3.

4.1.3 Glass-Sealing

As described, the glass-sealing is used in the initial cell construction process in order to join the IH with the BASE. Glass being an elastic material, once the joining operation is complete and the glass has fully solidified, the induced stresses below the T_s will be retained.

Much like the neighboring ceramics, glass is rigid in nature, and can more easily tolerate compressive stresses. Any induced tensile loading is undesired. Figure 4.6 shows the normal stress (with respect to the local curvature) distribution following the final cooling cycle from 350ºC to 20°C, where it was measured as a maximum. The expanded insert shows the innermost curved surface where the maximum normal stress was determined. The other surfaces of the glass-sealing were therefore omitted from treatment, due to their lower stress values, as evidenced in the figure.

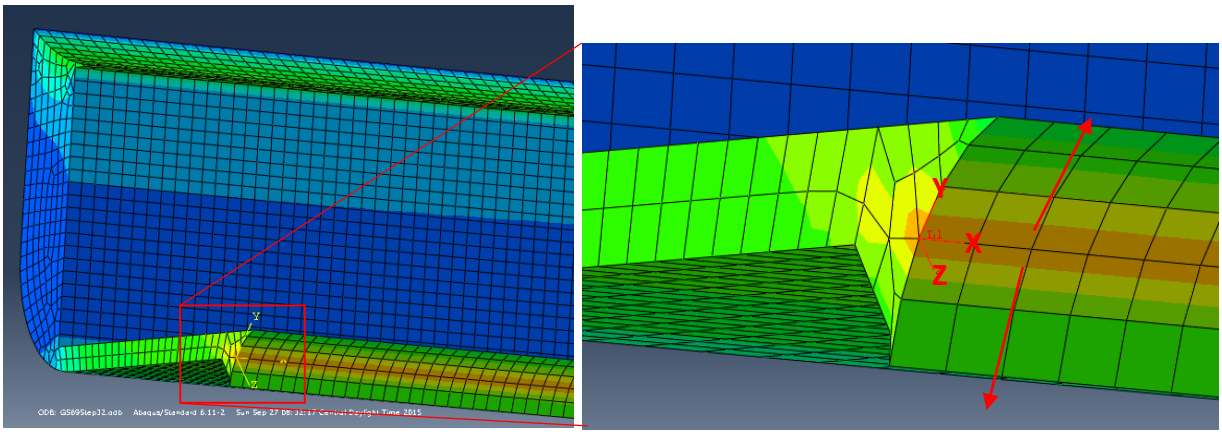

Fig. 4.6-Glass-sealing indicating the areas of maximum measured stresses in the normal direction.

The maximum localized normal stress on the inner-most curved surface of the glass-sealing following each computational cycle are summarized in Table 4.3, and the graphical representation created is shown in Figure 4.7. As indicated, the normal stress reaches a maximum after the final cooling cycle from 350°C (operational) to 20°C (room temperature).

Table 4.3-Maximum localized normal stresses on the surface of glass-sealing measured at the innermost curved surface in the standard planar-type cell following each of the three temperature cycles.

Stress Location	Measured Stress (MPa)		
	Step 1 520 – 20°C	Step 2 20 – 350°C	Step 3 350 – 20°C
GS Innermost Curved Surface Normal	21.41	-229.84	24.39

*: Negative Values indicate compressive stresses

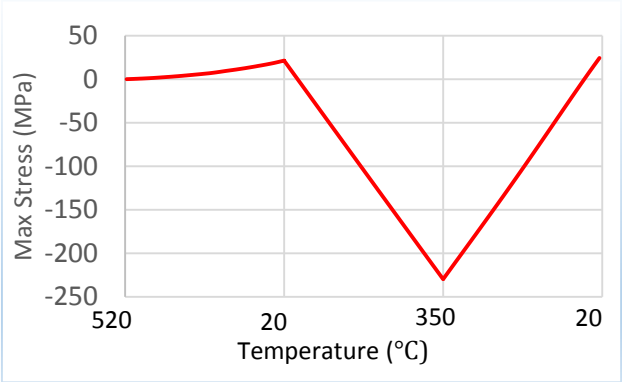

Fig. 4.7-Maximum localized inner-most curved glass-sealing normal stress plot using the standard three temperature cycle described further in Figure 4.3.

Similar to the plots obtained for the IH normal stresses, the shape of the resultant plot for the glass-sealing normal stress exhibits a similar trend (tensile → compression → tensile for steps 1, 2, and 3, respectively). The reasoning behind the resultant trend again due to the construction sequence during fabrication of the cell (see figure 4.3).

4.1.4 Beta-Alumina Solid Electrolyte (BASE)

The BASE is centrally located in the cell, and is inelastic in nature. Therefore, when the cell container materials are contracting around it during the cooling cycles, radial compressive stresses are induced. The maximum compression stresses in the radial direction were measured on the lower surface, as shown in Figure 4.8, as this surface retained greater compressive stresses in the radial direction (more negative).

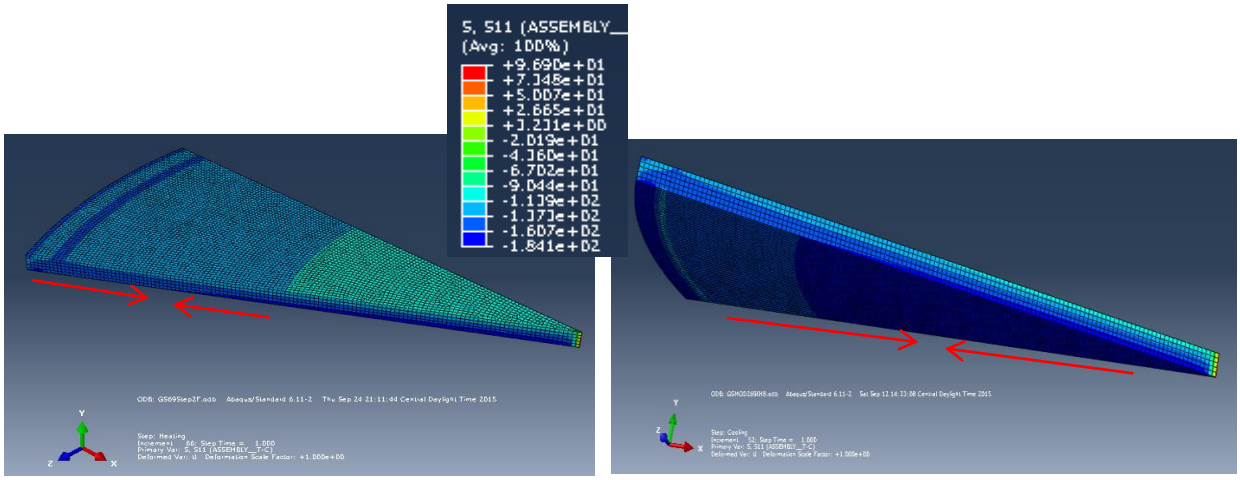

(a) **(b)**

Fig. 4.8-β-alumina electrolyte computational results indicating the areas of maximum measured normal stresses in the radial direction (most negative) on the **(a)** upper and **(b)** lower surfaces.

The maximum localized compressive stresses in the radial direction on the lower surface of the electrolyte were obtained following each computational step, and are summarized in Table 4.4, and the graphical representation created is shown in Figure 4.9. As indicated, the radial stress is a maximum following the heating cycle from 20 (room temp) to 350°C (operational), which is a direct consequence of the construction sequence shown in Figure 4.3.

Table 4.4-Maximum localized radial compressive stresses measured on the lower surface of the electrolyte, in the standard planar-type cell following each of the three temperature cycles.

Stress Location	Measured Stress (MPa)		
	Step 1 520 – 20°C	Step 2 20 – 350°C	Step 3 350 – 20°C
Lower Electrolyte Surface	-183.92	-1864.81	-211.426

*: Negative Values indicate compressive stresses

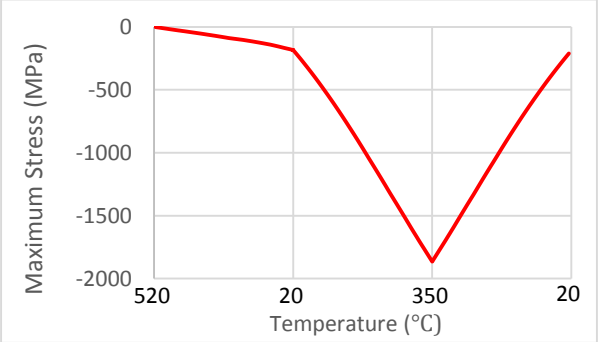

Fig. 4.9-Maximum localized radial stress plot using the standard three temperature cycle described further in Figure 4.3.

Similar to the plots obtained for IH, IM, and GS; the resultant graphical representation for the electrolyte radial compressive stress exhibits a similar trend, however the initial cooling cycle also has a negative slope. The reasoning again behind the resultant trend is due to the construction sequence during fabrication of the cell. The magnitude of the resultant radial compressive stresses (horizontal) are much higher than those experienced in the vertical normal measured in the other components. The electrolyte location at the center of the cell, is intuitively likely to experience the most severe compressive stresses.

4.1.5 General High-Stress Concentration Areas

Viewing the cell as a whole, several areas of localized stress concentrations are evident, as shown in Figure 4.10. The maximum stress locations in the **(a)** normal, **(b)** shear, and radial compressive **(c)** directions, in the standard 30° representative cell used for the majority of the computations are shown.

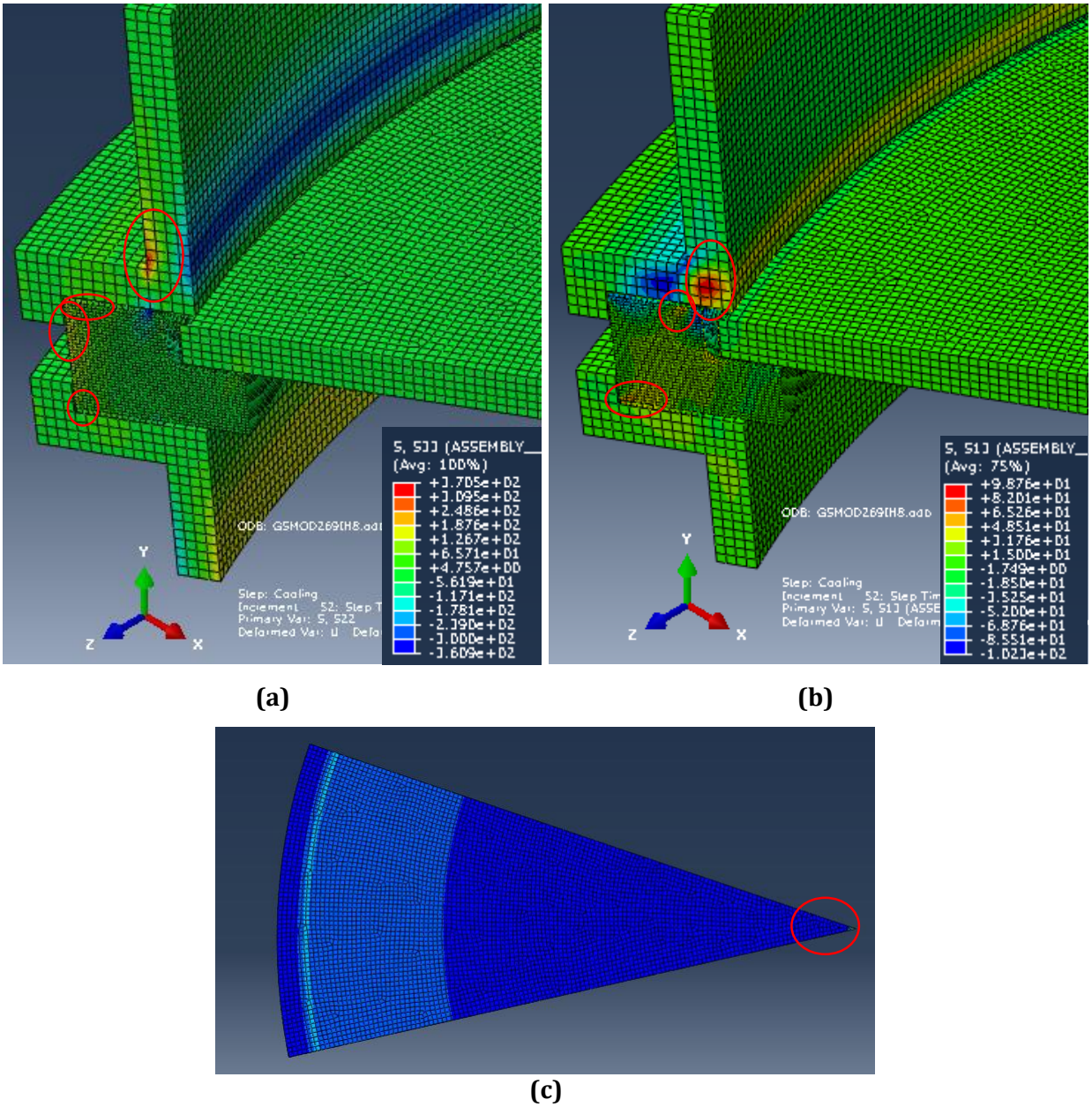

(a) **(b)**

(c)

Fig. 4.10-Computational results indicating the areas of maximum measured **(a)** vertical normal σ_{33}, **(b)** shear τ_{13}, and **(c)** radial compressive σ_{11} stresses in the 30° representative standard cell.

Following the initial cooling step, the previously discussed outside edge of the α-alumina IH indicates a region where elevated normal stresses were identified. Additionally, the addressed interfaces between the upper and lower IM and the IH near the outer edges are indicated in the normal direction as well. A significant stress concentration was also identified along the outer edge of the upper-collar near the upper bend radius. The specified STS431 is a plastically deformable martial however, with a much higher yield point than that of the adjacent Al inset metals. Therefore, the threat of failure due to the induced stress at this location is low, and the region was not further investigated.

In terms of shear stress concentrations, similar regions near the central insulating header insert metal interfaces were identified. A significant indication in the bulk of the upper collar appears to be the highest resultant shear stress location. A region just inside the edge of the upper Al3003 insert metal was also identified as containing elevated shear stresses.

As discussed previously, the radial compressive stresses are highest in the electrolyte based upon its central location in the cell. All of the surrounding metallic components are contracting in on the electrolyte. The maximum compressive stress site was located near the center of the electrolyte, on the lower surface.

4.2 Impacts of Glass-Sealing CTE Variations

Until now, we only discussed the stress concentrations in the standard (control) NaS cells. From this point, we attempted to alter the material properties and cell design variables, as mentioned earlier. The initial computational trials focused on varying the CTE values of

the glass-sealing material. The CTE value used during congruent prototyping was measured and reported by RIST as $6.9E^{-6}K^{-1}$. To test the impacts of CTE values of glass on the stress accumulation in adjoining insulating header and electrolyte ceramics, the values chosen ranged from $5.0E^{-6}K^{-1}$ to $8.0E^{-6}K^{-1}$. Specifically, values of 5.0, 6.0, 6.9, & $8.0E^{-6}K^{-1}$ were used for the computations in the standard cell described prior. To reserve computational resources, the experimental trials included stress analysis for the initial cooling cycle only. This decision was also based upon the gathered results from the standard cell computations. The results based upon the glass-sealing variance are therefore presented with the three temperature cycles for the standard (control) cell only.

The same interfaces and individual component surfaces were analyzed for the glass-sealing CTE variance trials, and as Figure 4.11 indicates, the only significant differences in measured stresses occurred at the inner insulating header vertical surface. In the figure, the data gathered for the standard cell is shown in gray, while the other colors represent the aforementioned CTE value modifications. A slight variance in the inner-most curved glass-sealing normal stresses was also noted in the figure. These regions were more closely analyzed, as follows.

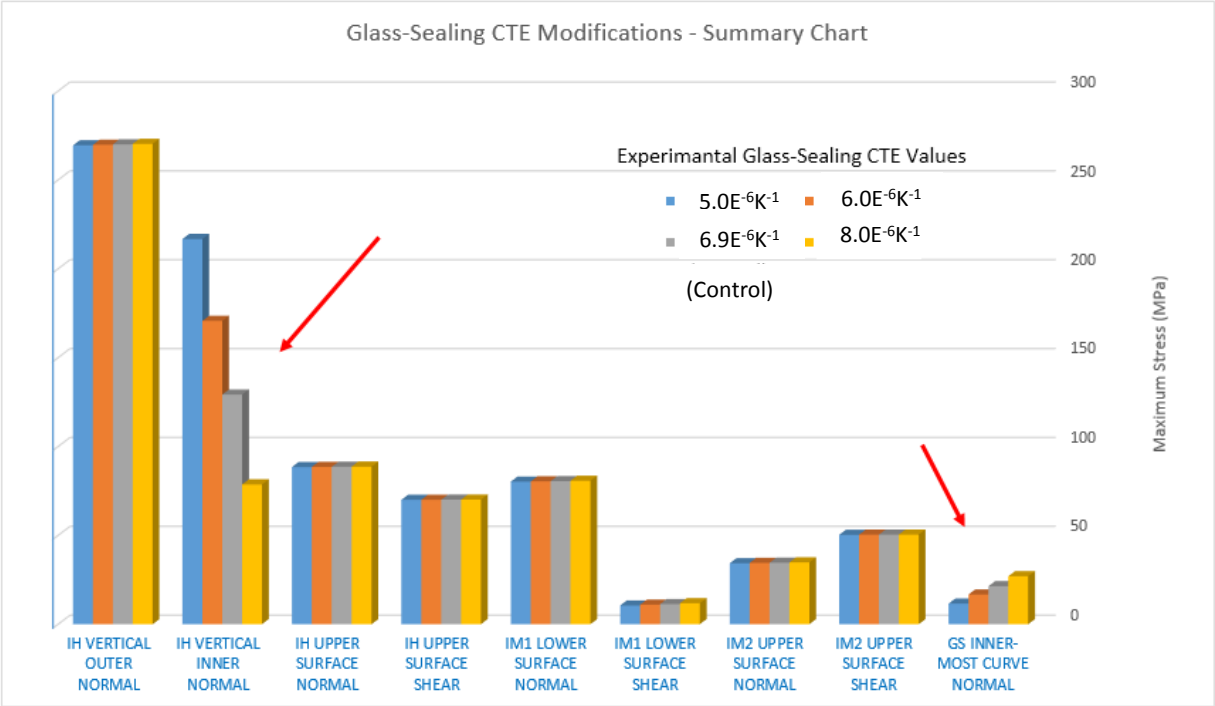

Fig. 4.11-Localized maximum measured stresses for the glass-sealing variation trials at the various locations listed in blue below the x-axis.

Only minimal stress differences were evident at the other locations; however, the variance from 79 to 217 MPa at the inner vertical surface was significant. The measured values at the inner vertical surface for each of the glass-sealing CTE variance cells is documented in Table 4.5, and shown visually in Figure 4.12.

Table 4.5-Localized normal stresses measured at the innermost vertical surface of the insulating header following the initial cooling cycle (520 - 20°C).

Normal Stress Location	Measured Stress (MPa)			
	GS CTE of $5.0E^{-6}K^{-1}$	GS CTE of $6.0E^{-6}K^{-1}$	GS CTE of $6.9E^{-6}K^{-1}$ (Control)	GS CTE of $8.0E^{-6}K^{-1}$
Inner-Vertical Header Surface	216.73	170.66	129.23	78.65

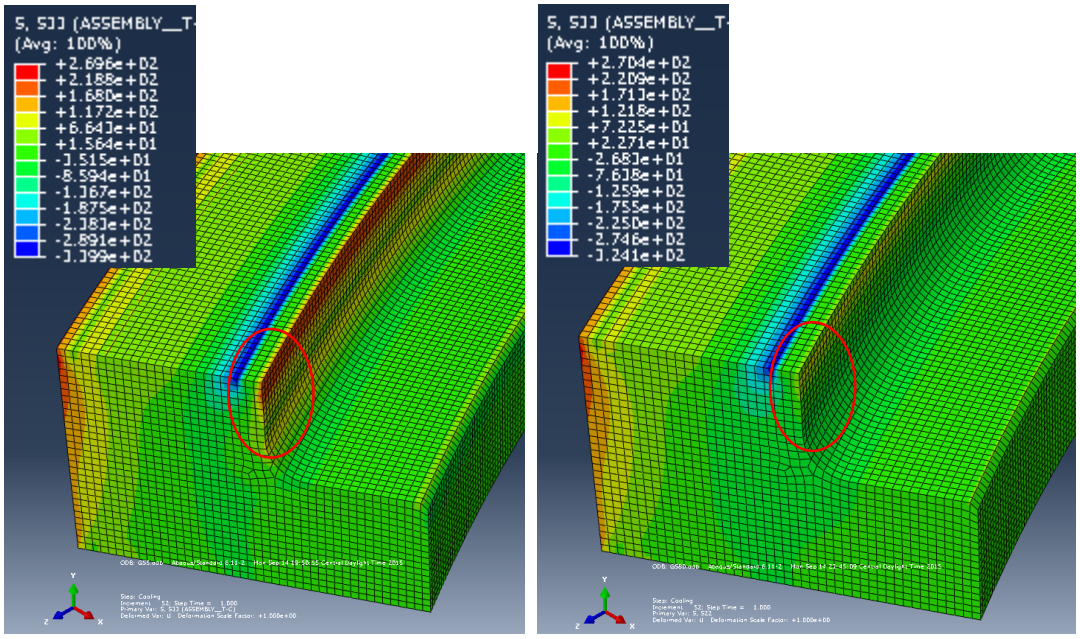

(a) **(b)**

Fig. 4.12-Computational results indicating the areas of maximum measured normal stresses in the insulating header from **(a)** $5.0E^{-6}K^{-1}$ and **(b)** $8.0E^{-6}K^{-1}$ glass-sealing CTE cells.

The left image **(a)** shows the cell containing the glass-sealing with a specified CTE value of $5.0E^{-6}K^{-1}$, where the maximum inner normal stresses were measured. The right image **(b)** shows the same stress distribution in the cell containing the glass-sealing with a specified CTE value of $8.0E^{-6}K^{-1}$. As the plot in Figure 4.13 indicates, the stress reduction on the insulting header inner vertical surface was significant. It is, however, important to note that although a maximum of 217 MPa was documented on the inner vertical surface, the outer vertical surface was still subjected to higher stresses, which remained similar (approximately 270 MPa) across the entire glass-sealing CTE variance range.

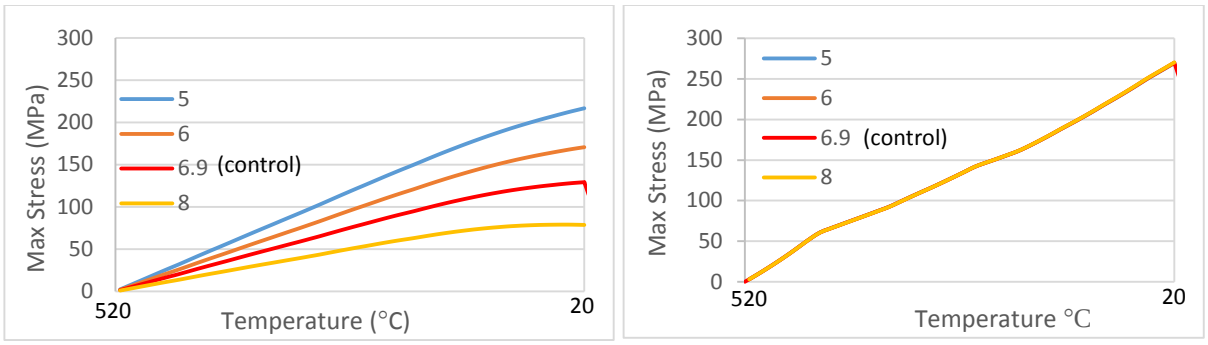

(a) **(b)**

Fig. 4.13-Computational results with different glass-sealing CTE values on the **(a)** inner insulating header surface and **(b)** outer header surface. The 5 through 8 in the legends refer to values of 5.0E-^{6}K^{-1} through 8.0E-^{6}K^{-1} glass-sealing CTE values.

The only other significant stress concentration differences influenced by the glass-sealing CTE modifications was identified at the glass-sealing inner-most curved normal stress. Although not as drastic an influence as the inner insulating header stresses, the glass-sealing normal had a range of approximately 12 MPa in the lowest 5.0E-^{6}K^{-1} CTE trial, to a maximum of approximately 27 MPa for the 8.0E-^{6}K^{-1} CTE trial, respectively. A graphical summary showing the measured stresses in the normal direction on the inner-most curved surface is shown in Figure 4.14 following the initial cooling cycle.

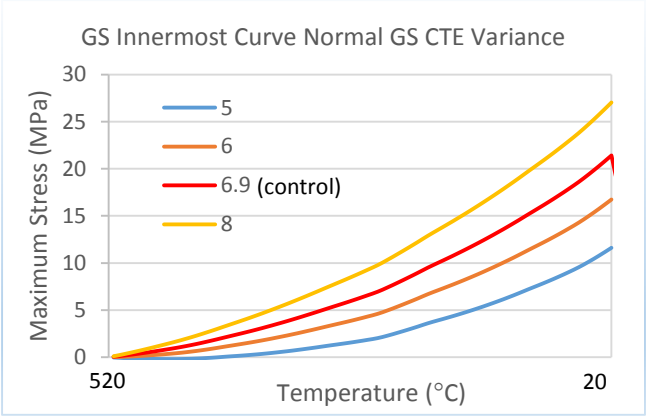

Fig. 4.14-Computational results with different glass-sealing CTE values on the inner-most glass-sealing curved surface normal stresses. The 5 through 8 in the legend refer to values of 5.0E-^{6}K^{-1} through 8.0E-^{6}K^{-1} CTE values.

4.3 Impacts of Container Metal CTE Variations

As described in Chapter 3, in this particular trial, the impacts of the CTE values of the outer STS431 container were investigated. Shown in Figure 4.15, the chosen CTE values for the experimental variables were not constants, instead, they were varied proportionally with the standard cell CTE curve (blue). The modifications were made to more closely align with that of the α-alumina CTE curve (yellow), in an attempt to reduce the resultant stress values determined in the standard cell trial (section 4.1). In the work herein, the curves will be referred to by their approximate numerical averages (i.e., 11 [control], 10, and 9).

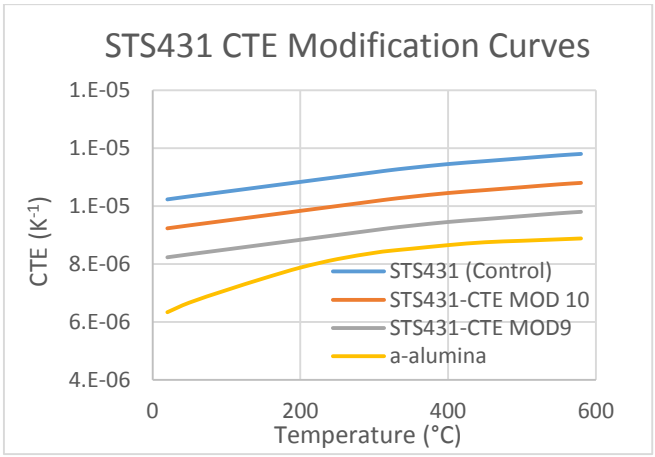

Fig. 4.15-The standard CTE curves with respect to temperature for STS431 (blue) and α-alumina (yellow), in addition to the two CTE variable curves chosen (orange & gray).

In contrast to the negligible differences of the glass-sealing CTE modifications on the resultant stresses, the localized maximum stresses at most of the analyzed regions exhibited greater variance when the container material CTE curves shown in Figure 4.15 were implemented. The stainless steel CTE container material modification trials indicated the most influence at the outer vertical surface of the electrical insulating header, where the

overall maximum stress was identified in the standard cell. In contrast to the glass-sealing CTE modifications, only minimal variance at the inner vertical header surface was evident. Figure 4.16 summarizes the maximum localized stresses measured at the same regions analyzed prior for the standard and glass-sealing CTE modification trials documented prior.

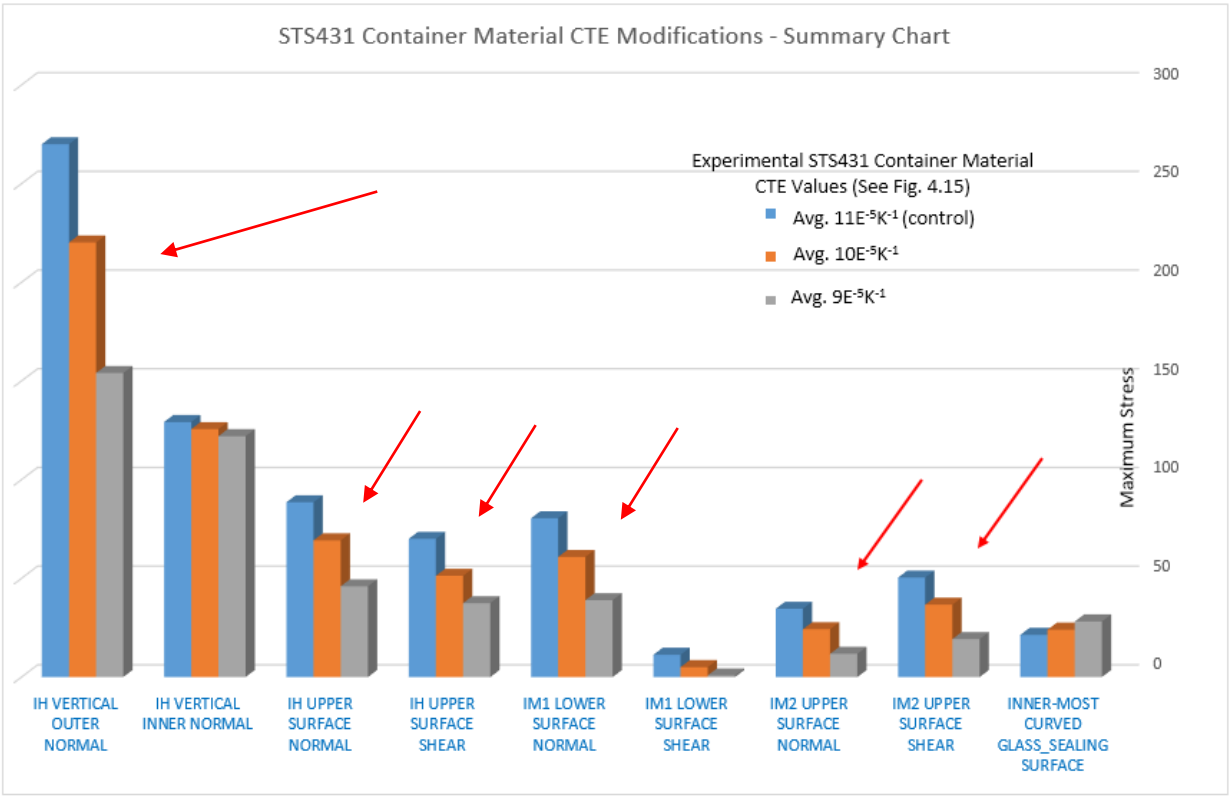

Fig. 4.16-Localized maximum measured stresses for the STS431 container material variation trials.

Stress differences based upon the cell container CTE variations were evident in nearly all of the measured regions, and intuitively exhibit a downward trend as the CTE of the cell container more closely resembles that of the α-alumina insulating header. The only noted exceptions were a general lack of variance at the inner vertical insulating header surface, the lower shear stresses on the upper insert metal, and a slightly positive (opposite) trend at the innermost curved glass-sealing surface. The measured values at the outer vertical surface

for each of the cell container CTE variance cells is documented in Table 4.6, and shown visually in Figure 4.17.

Table 4.6-Localized normal stresses measured at the outer most vertical surface of the insulating header following the initial cooling cycle (520 - 20°C).

Normal Stress Location	Measured Stress (MPa)		
	Average STS CTE of 11.0E^{-5}K^{-1} (Control)	Average STS CTE of 10.0E^{-5}K^{-1}	Average STS CTE of 9.0E^{-5}K^{-1}
Outer Vertical Header Surface	269.99	220.20	154.08

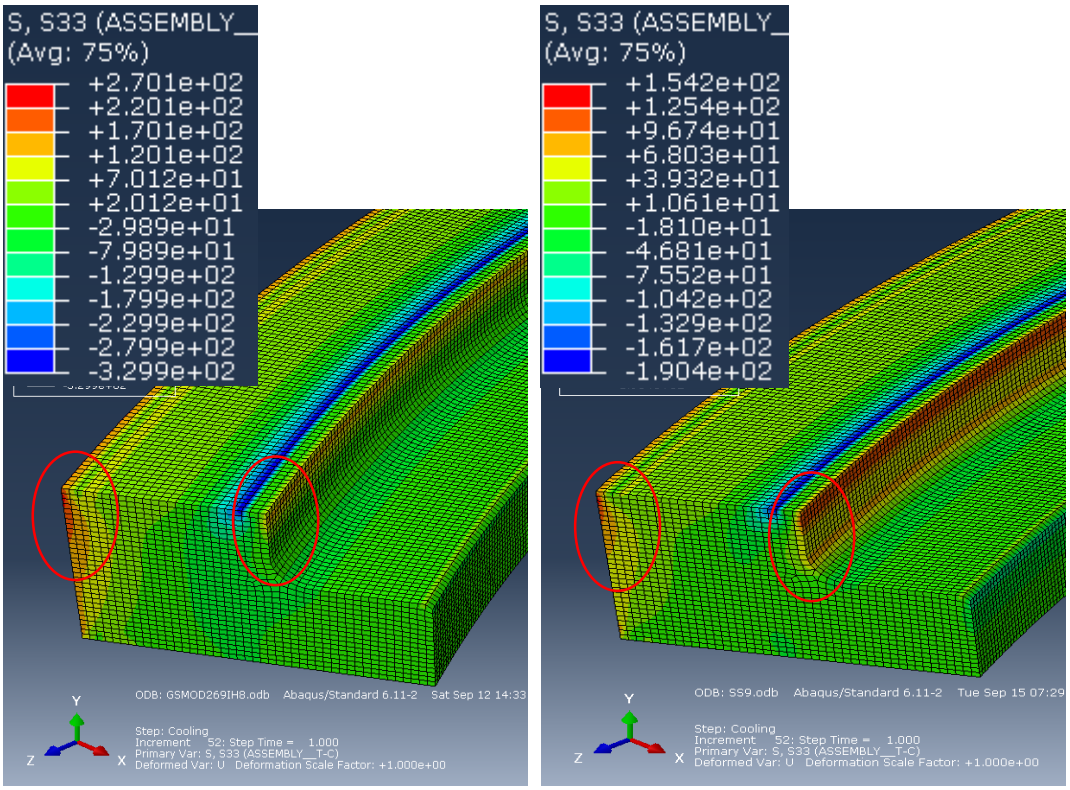

(a) **(b)**

Fig. 4.17-Computational results indicating the areas of maximum measured normal stresses in the average **(a)** 11E^{-5}K^{-1} (standard) and **(b)** 9E^{-5}K^{-1} container CTE cells.

As anticipated, the merger of the CTE curves between the stainless steel cell containers with that of the α-insulator header, resulted in a reduction of resultant induced tensile stresses. The more significant reduction was at the outer vertical surface, and the resultant graphical representation is shown in Figure 4.18. The maximum measured stress at the outer IH was nearly reduced by half when the container CTE curve with an average of $9.0E^{-5}K^{-1}$ was implemented. The additional normal and shear stresses at the upper IH were also reduced, however, not as drastically. The magnitude of these stresses were much lower in relation to those measured at the outer vertical surface as well, so further treatment is not given here.

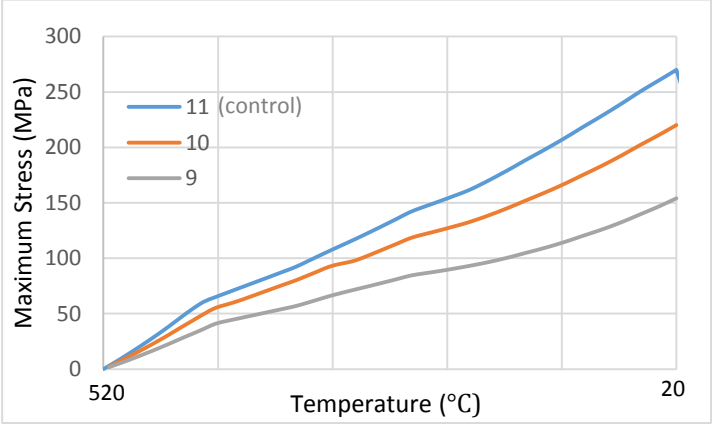

Fig. 4.18-Computational results with different container CTE values on the outer insulating header surface normal stresses. The 11 through 9 in the legend refer to average CTE values of $11E^{-5}K^{-1}$ through $9E^{-5}K^{-1}$ (See Fig. 4.15).

The magnitudes of the resultant stresses at the upper and lower IM followed the same trend as those documented in the glass-sealing CTE trials, with an overall reduction of the localized stresses at each interface as the container CTE values were reduced. Table 4.7 lists the localized normal and shear stresses at the various insert metal surfaces as a function of

the chosen CTE values. As shown, the stress at the lower surface of the upper IM was nearly completely eliminated following the initial cooling step from 520 – 20 °C. Again, to conserve computational resources, data for the container CTE variance trials was only obtained following the initial cooling step. The corresponding resultant graphical representations are shown in Figure 4.19.

Table 4.7-Measured localized normal and shear stress values obtained from the upper and lower insert metals in the container CTE variance cells following the initial (520-20°C) temperature cycle.

Component	Measured Stress (MPa)			
	Surface	Average STS CTE of $11E^{-5}K^{-1}$(Control)	Average STS CTE of $10E^{-5}K^{-1}$	Average STS CTE of $9E^{-5}K^{-1}$
Upper Insert Metal 1	Lower Normal	80.52	60.91	39.00
	Lower Shear	11.28	5.06	0.86
Lower Insert Metal 2	Upper Normal	34.62	24.25	11.81
	Upper Shear	50.45	36.74	19.30

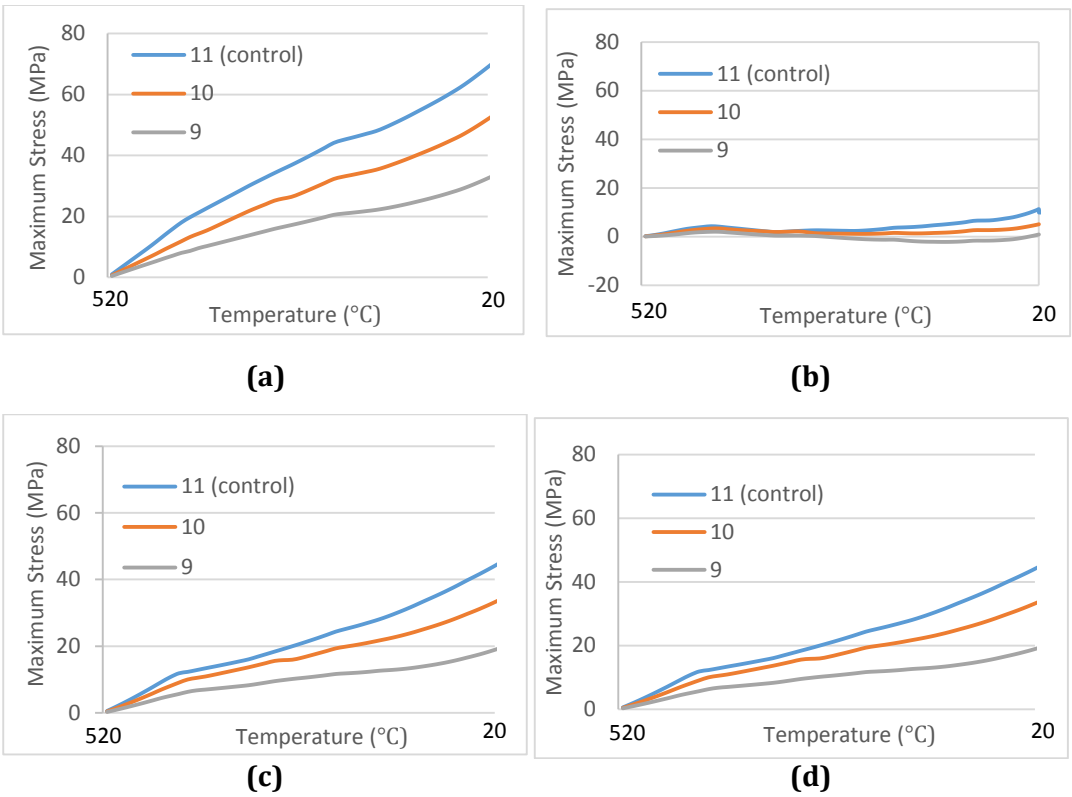

Fig. 4.19-Computational results with different container CTE values on the **(a)** IM1 lower normal stress, **(b)** IM1 lower shear stress**, (c)** IM2 upper normal, and **(d)** IM2 upper shear. The 11 through 9 in the legends refer to the average values of $11.0E^{-5}K^{-1}$ through $9.0E^{-5}K^{-1}$ container CTE values (See Fig. 4.15).

The only other stress differences influenced by the container CTE modifications were at the glass-sealing inner-most curved normal. Although not as drastic an influence as the inner insulating header stresses, the glass-sealing normal had a range of approximately 21 MPa in the lowest $11E^{-5}K^{-1}$ CTE trial to a maximum of approximately 28 MPa for the $9E^{-5}K^{-1}$ CTE value, respectively. A graphical summary showing the measured stresses in the normal direction on the inner-most curved surface is shown in Figure 4.20.

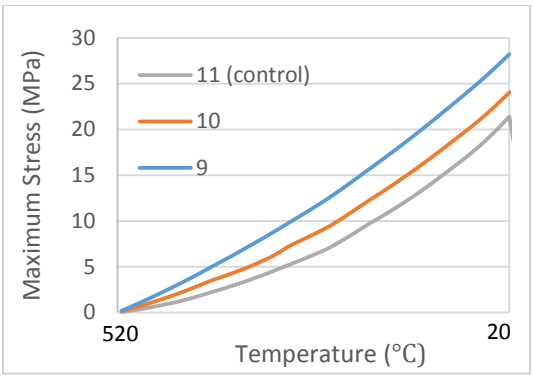

Fig. 4.20-Computational results with different container CTE values on the innermost glass-sealing curved surface normal stresses. The 11 through 9 in the legend refer to average values of $11E^{-6}K^{-1}$ through $9E^{-6}K^{-1}$ CTE values chosen (See Figure 4.15).

4.4 Impacts of Insert Metal Thickness Variations

In addition to material CTE variations, exploration into potential geometrical dimensional modification trials were also performed. Namely, the thickness of the IM and outer container materials were chosen based on the maximum stress concentrations that were previously determined. The IM thickness in the standard cell is 0.25mm. The modifications were chosen as a 25% variance in either direction, namely, 0.1875mm and 0.3125mm. Based on the resultant computational data, the same surfaces were analyzed for any significant changes in thermally induced stresses, as summarized in Figure 4.21. In general, no huge differences in the measured stresses were identified through the IM thickness trials.

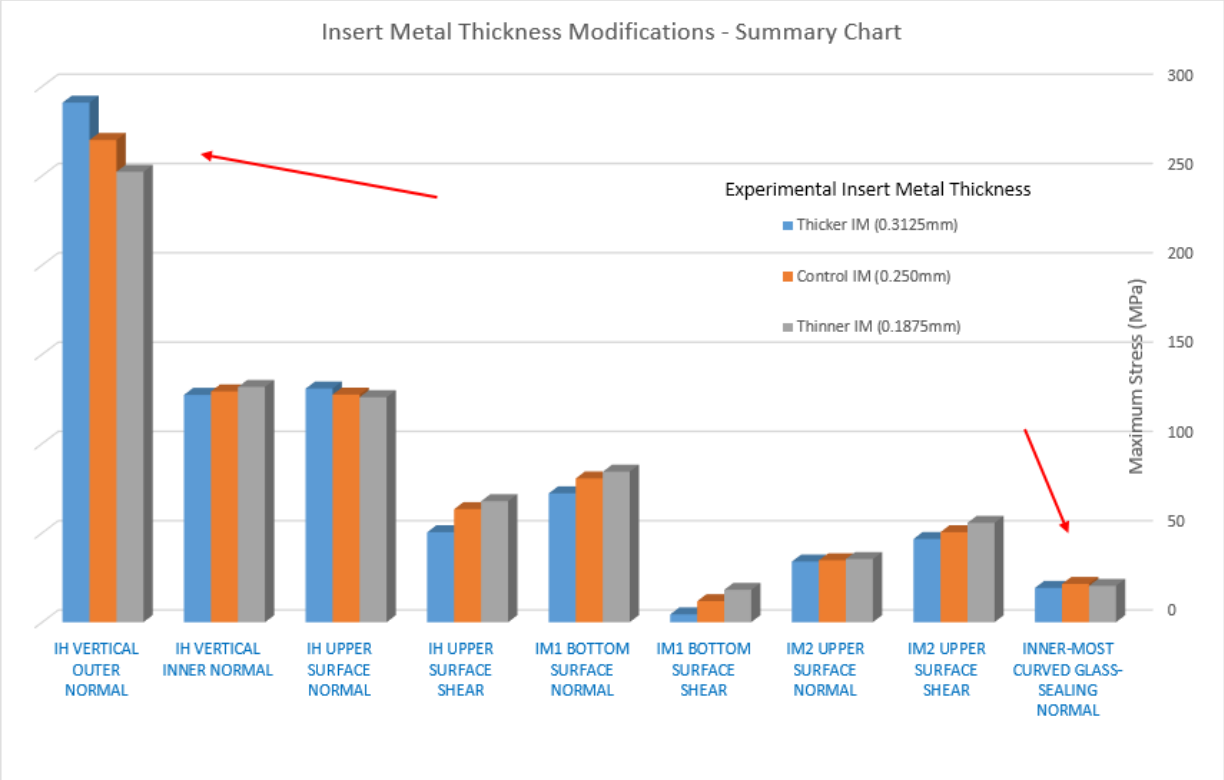

Fig. 4.21-Localized maximum measured stresses for the IM thickness variation trials.

The outer vertical IH surface showed the greatest variance, and the results were as anticipated. When the thickness of IM was reduced, the resultant measured normal stress at the outer most vertical header surface also decreased. Likewise, when the thickness was increased, the resultant stress was increased. The measured values at the outer vertical surface for each of the Al insert metal thickness modification cells are documented in Table 4.8, following the initial cooling cycle from 520 - 20°C, and they are shown visually in Figure 4.22.

Table 4.8-Localized normal stresses measured at the outer most vertical surface of the insulating header following the initial cooling cycle (520 - 20°C).

Normal Stress Location	Measured Stress (MPa)		
	Thinner 0.1875mm	Control Cell 0.25mm	Thicker 0.3125mm
Outer Vertical Header Surface	252.20	269.99	290.89

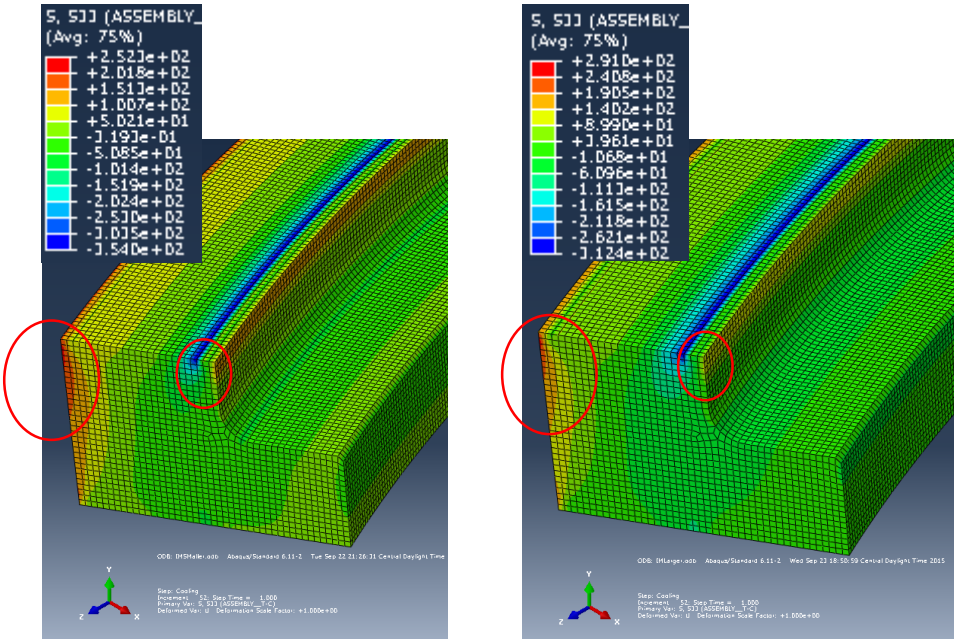

(a) **(b)**

Fig. 4.22-Computational results indicating the areas of maximum measured normal stresses in the **(a)** reduced IM thickness cell and **(b)** increased IM thickness cell.

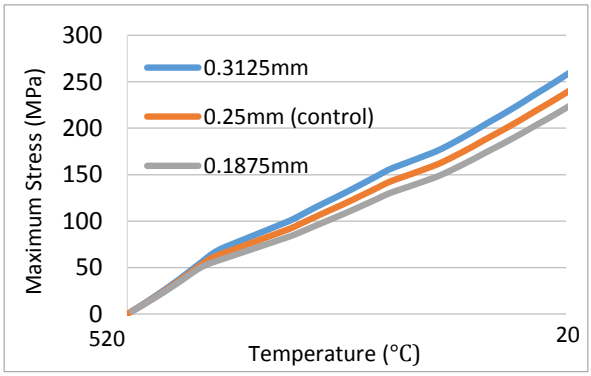

Fig. 4.23-Computational results with different IM thicknesses on the outer insulating header surface normal stresses.

The more significant reduction was at the outer vertical surface of the IH, and the resultant graphical representation is shown in Figure 4.23. The maximum measured stress at the outer IH was reduced by just under 20MPa, when the IM thickness was reduced to 0.1875mm, and increased around 20MPa when the thickness was increased to 0.3125mm. Only the upper normal surface exhibited this same trend, and the additional normal and shear stresses measured for these trials exhibit a positive trend as the IM thickness was decreased. The magnitudes of these stresses were much lower than those measured at the outer vertical surface as well, and not much variance was induced between trials. Therefore, further treatment is not given here. The inner most glass-sealing trend was somewhat interesting, as a maximum in measured normal stress was actually highest in the standard cell. Both a reduction and increase in thickness resulted in a slightly lower induced stress at this location. It should be noted however, that the magnitudes of all three cells were within 2MPa of one another, and therefore the differences are insignificant, and within the anticipated error tolerance.

4.5 Impacts of Container Thickness Variations

This section will address the outer container metal thickness modifications. The container metal thickness in the standard cell is 2mm. The modifications were chosen 25% in either direction, namely, 1.5 and 2.5mm. Based on the resultant computational data, the same surfaces were analyzed for any significant changes in thermally induced stresses, as summarized in Figure 4.24. In general, the container thickness modifications contributed to the largest variances at nearly every location, of any of the cell modifications performed.

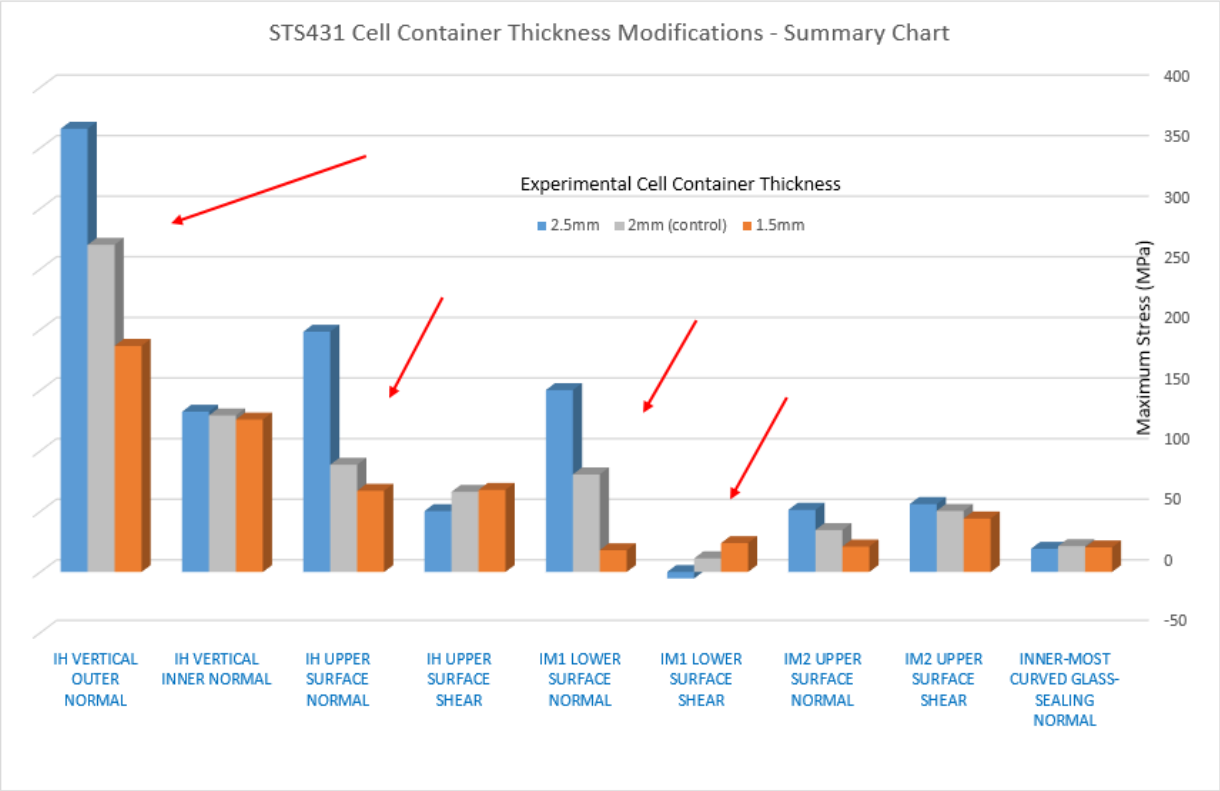

Fig. 4.24-Localized maximum measured stresses for the outer container metal thickness variation trials.

As was the case in many of the trials prior, the outer vertical IH surface showed the greatest variance, and the results were as anticipated. When the thickness of the container material was reduced, the resultant measured normal stress at the outer most vertical header surface also decreased. Likewise, when the thickness was increased, the resultant stress was increased. The measured values at the outer vertical surface for each of the outer container metal thickness modification cells are documented in Table 4.9 following the initial cooling cycle from 520 - 20°C, and they are shown visually in Figure 4.25.

Table 4.9-Localized normal stresses measured at the outer most vertical surface of IH following the initial cooling cycle (520 - 20°C).

Normal Stress Location	Measured Stress (MPa)		
	Thinner 1.5mm	Control Cell 2.0mm	Thicker 2.5mm
Outer Vertical Header Surface	186.56	269.99	365.81

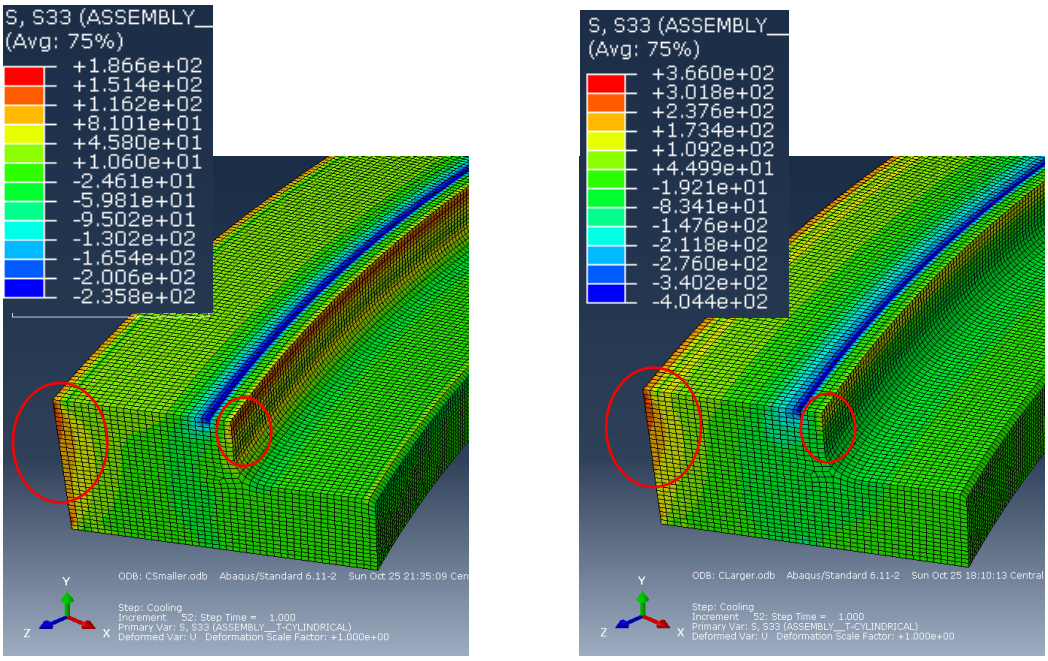

(a) **(b)**

Fig. 4.25-Computational results indicating the areas of maximum measured normal stresses in the **(a)** reduced container thickness cell and **(b)** increased container thickness cell.

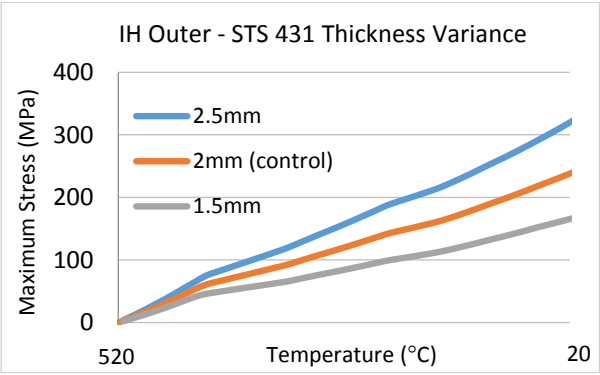

Fig. 4.26-Computational results with different container thickness values, on the outer IH surface normal stresses.

The more significant reduction was at the outer vertical surface, and the resultant graphical representation is shown in Figure 4.26. The maximum measured stress at the outer IH was reduced by ~100MPa when the collar container thicknesses were reduced to 1.5mm, and increased by ~100MPa when the thickness was increased to 2.5mm, respectively. Almost all of the additional surfaces followed a similar negative trend as the container thickness was reduced, and the increase in thickness greatly elevated the resultant stresses, while the reduction contributed to a lesser extent.

Only the upper IH normal stress, the upper IM shear, and innermost glass-sealing normal stresses exhibited a positive trend, as the container thickness was reduced. The magnitudes of these stresses were much lower than those measured at the outer vertical surface as well, and not much variance was induced between trials. Additionally, a negative, or compressive stress, was induced at the upper IM/IH interface when the container thickness was increased to 2.5mm. A trend that was only witnessed during this single trial. The results of these trials were generally in line with the previously described IM thickness variance trials, and in comparison with other neighboring surfaces, the stress magnitudes were low. Therefore, further treatment was not given.

Again, the innermost glass-sealing trend was somewhat interesting, as a maximum in measured normal stress was actually highest in the standard cell. Both a reduction and increase in thickness resulted in a slightly lower induced stress at this location. It should be again noted, however, that the magnitudes of all three cells were within 2MPa of one another, and therefore the differences are insignificant, and within the anticipated error tolerance.

The interface between the IH and upper IM was of special concern as well. Like the outer IH normal, the thicker container material had significant effect on the resultant stresses. The resultant plots from this interface are shown in Figure 4.27 for further visual clarification.

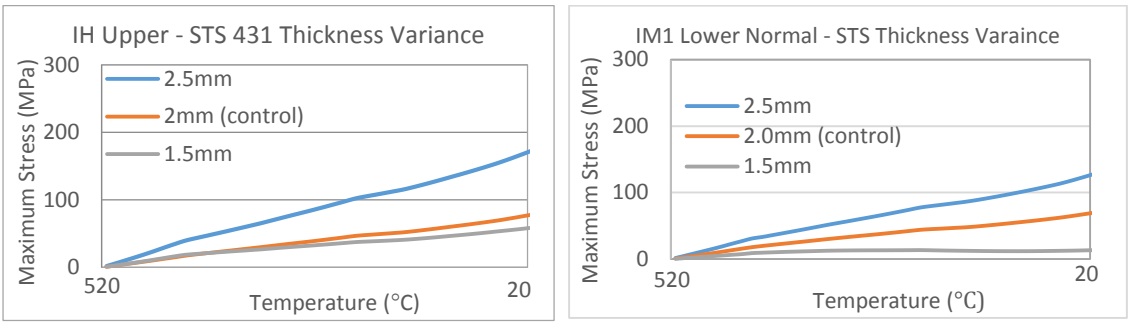

(a) **(b)**

Fig. 4.27-Computational results with different STS431 container thicknesses on the **(a)** upper IH surface normal stress and **(b)** mating upper IM normal.

4.6 Electrolyte Centering Issue

The glass-sealing joining process is a crucial part of the cell construction, which must be treated carefully. As discussed prior, the electrolyte itself is a thin β-alumina ceramic, which is extremely fragile. Centering of the electrolyte at the region within the α-alumina IH could be of high significance. This final trial was conducted to investigate the resultant stress concentrations if the electrolyte disk was not properly centered during the glass-sealing operation. Some simplifications were made in carrying out the model development for this particular cell. For these trials, a 180° half-cell was required to study the effects of the electrolyte centering issues. The model developed and used for these trials is shown in Figure 4.28.

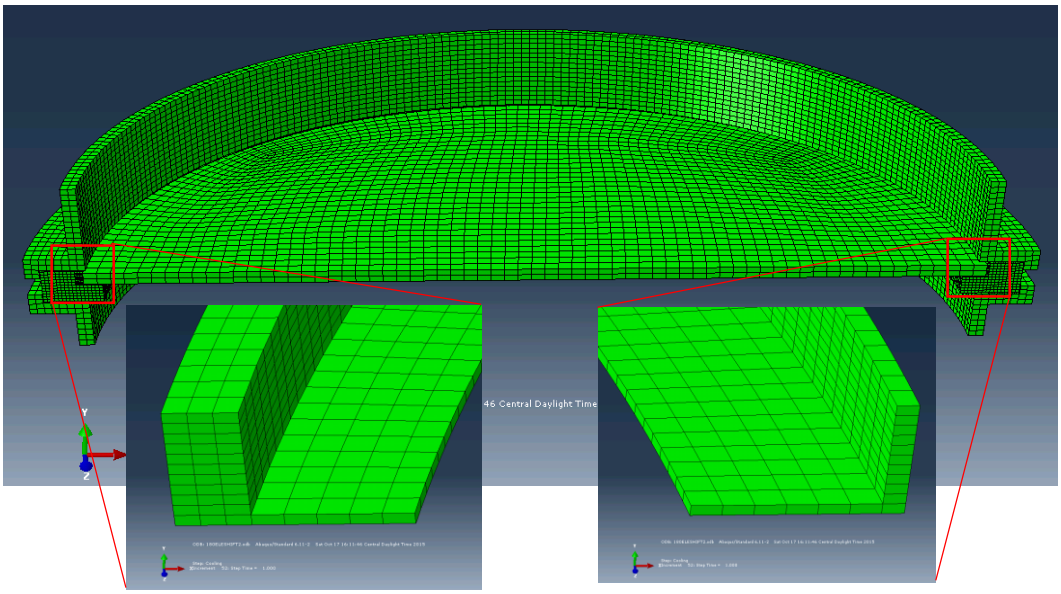

Fig. 4.28-The 180° half-cell used for the electrolyte centering trials. The inserts show the larger (1.073mm) and smaller (0.358mm) glass-sealing thicknesses which are 180° apart. The electrolyte was shifted 50% of the standard thickness of 0.715mm.

As shown in the figure, the electrolyte was shifted ~50% of the original glass-sealing thickness of 0.715mm. Thus, resulting in a thicker glass-sealing of 1.073mm, and a thinner glass-sealing thickness of 0.3585mm. After the initial cooling step, the corresponding areas of interest based upon the previously conducted work is shown for both the normal and shear directions in Figure 4.29. The stress concentrations are similar to those found in the previous trials, although the simplifications in geometry are evident.

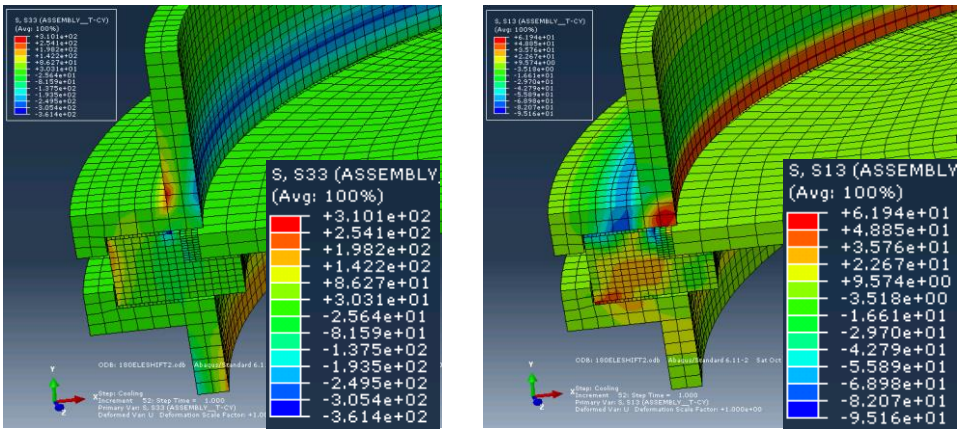

(a) **(b)**

Fig. 4.29-Computational results indicating the areas of maximum measured **(a)** vertical normal σ_{33}, and **(b)** shear τ_{13}, in the 180° representative modified electrolyte shifted cell.

For this trial, only the glass-sealing and electrolyte components were investigated to determine the influence of the electrolyte shift. Namely, the upper glass-sealing normal stress (vertical), glass-sealing upper radial compressive normal (horizontal), lower horizontal glass-sealing shear stress, and radial compression electrolyte stresses were measured. Table 4.10 indicates the results from the four locations analyzed, and Figure 4.30 summarizes the data graphically. As done in the previous trials, the electrolyte compression data was not included in the plot to more clearly show the trends of the other localized stress locations.

Table 4.10-Summary of localized maximum measured stresses for the electrolyte shift trial.

Component	Measured Stress Location	Measured Stress (MPa)					
		Step 1 520 – 20°C		Step 2 20 – 350°C		Step 3 350 – 20°C	
		Thicker GS	Thinner GS	Thicker GS	Thinner GS	Thicker GS	Thinner GS
Glass-Sealing	Upper Normal	8.32	-87.05	-243.78	-339.14	8.32	-105.65
	Electrolyte Interface Shear	16.21	14.87	16.21	14.86	16.21	14.86
	Upper Radial Compression	-86.85	-184.1	-338.94	-436.19	-86.84	-184.08
Electrolyte	Lower Radial Compressive	-167.64	-168.93	-1851.40	-1852.59	-1667.65	-168.90

*: Negative values indicate compressive stresses

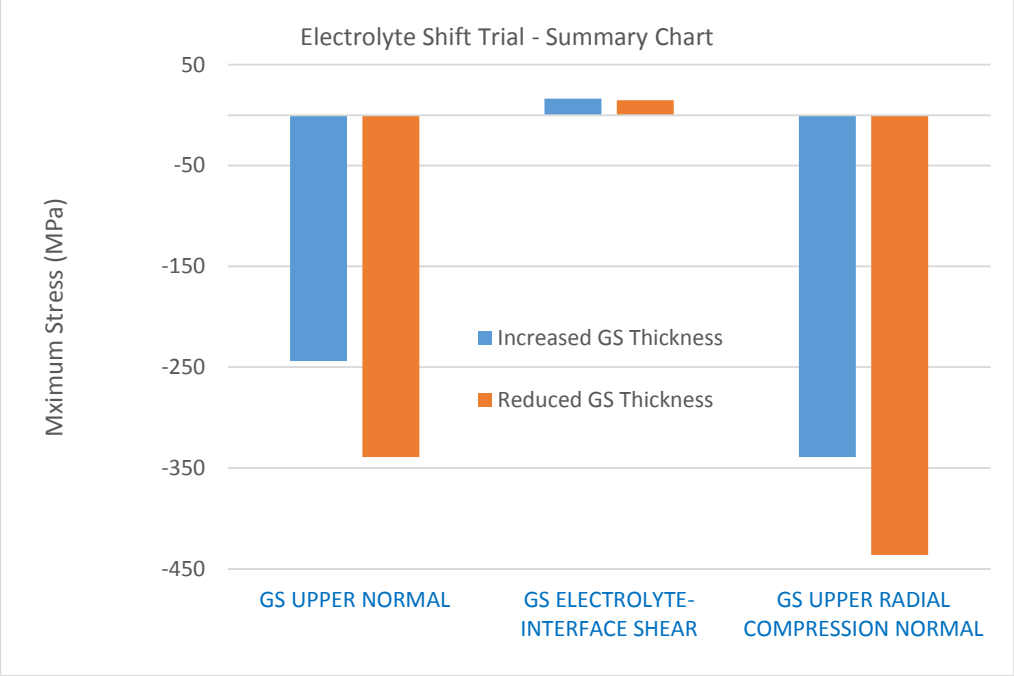

Fig. 4.30-Selected localized maximum measured stresses for the electrolyte shift investigation trial.

The majority of the measured normal and shear stress maximums were negative, indicating compressive stresses in the glass and ceramic materials. The measured normal

stresses on the glass-sealing component surfaces were reduced (less negative) at the thicker glass-sealing location. The positive shear stress values measured on the glass-sealing surface at the electrolyte interface are of concern however. Although not much variance was evident between the induced shear stress on either side of the glass-sealing, the positive values indicate tensile loading that can contribute to premature failure.

Plots of the glass-sealing upper normal and upper shear values obtained from the electrolyte interface more clearly depict the differences induced at the thicker and thinner glass-sealing locations. The plots are shown below in Figure 4.31, which indicate similar trends.

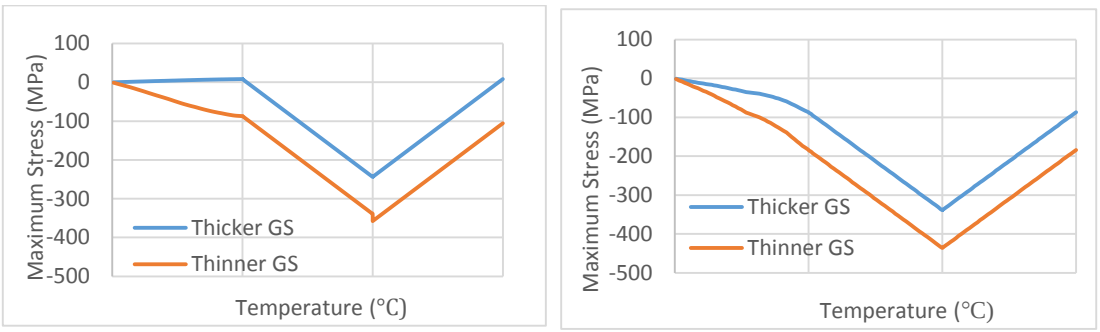

Fig. 4.31-Computational results of the electrolyte shift on the **(a)** upper glass-sealing normal stress and **(b)** electrolyte interface normal stress.

In Figure 4.32, the resultant glass-sealing at both sides to more clearly indicate the region of potential tensile loading. Here, the resultant normal direction distributions are also shown for both the vertical and horizontal directions over the heating cycle (20 - 350°C), where the stresses were measured at a maximum.

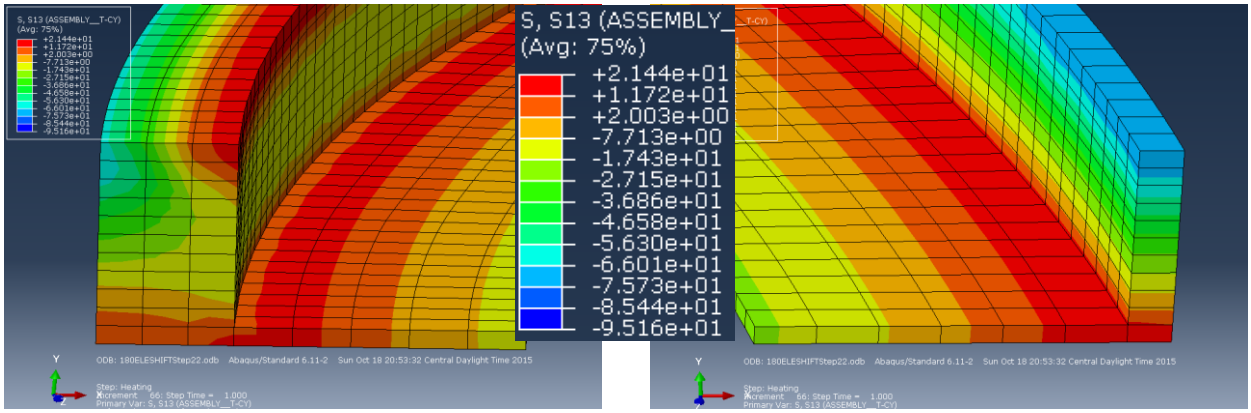

(a)

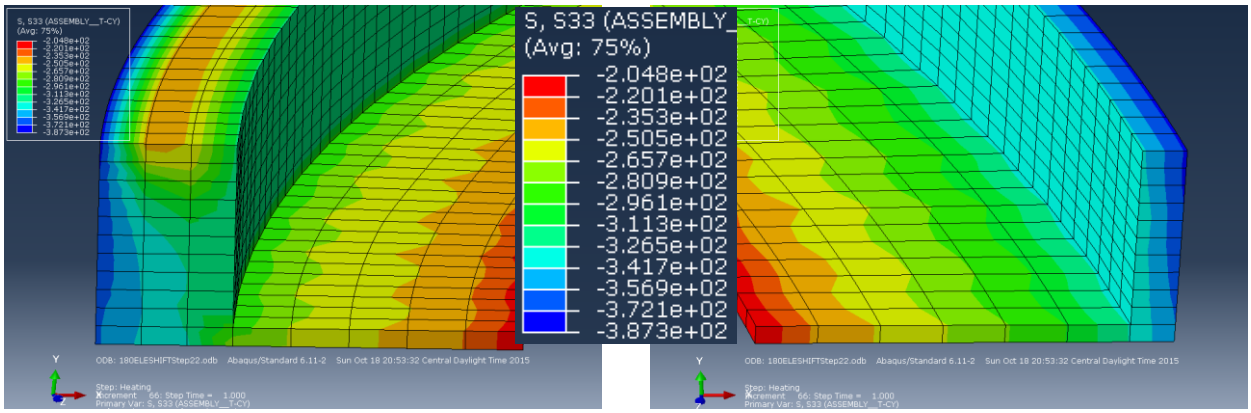

(b)

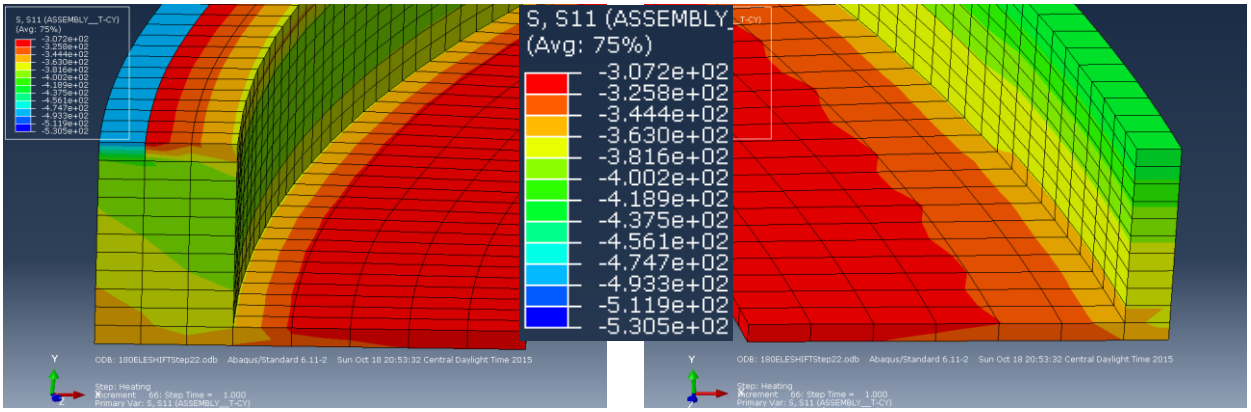

(c)

Localized maximum stresses in the glass-sealing following the heating cycle from 20 - 350°C, **(a)** in the horizontal shear τ_{13} direction, **(b)** vertical normal σ_{33} direction, and **(c)** horizontal σ_{11} normal compressive direction.

As Table 4.10 outlined, the stress variation in the electrolyte was also analyzed, and it was determined, as in the standard cell, that the maximum radial compressive stresses (σ_{11}) were also evident following the heating cycle from 20 - 350°C. Although the geometry of the cell was modified slightly to incorporate the electrolyte shift, the magnitudes measured on the lower electrolyte surface were similar to those observed from the standard cell (-1865 vs. -1867 MPa respectfully). Additional localized maximums at the glass-sealing interfaces on each side were also nearly equal. A slight decrease by approximately 1MPa was evident at the reduced glass-sealing thickness region. A resultant image of the lower electrolyte surface following the heating cycle from 20 - 350°C is shown for visual aid in Figure 4.33.

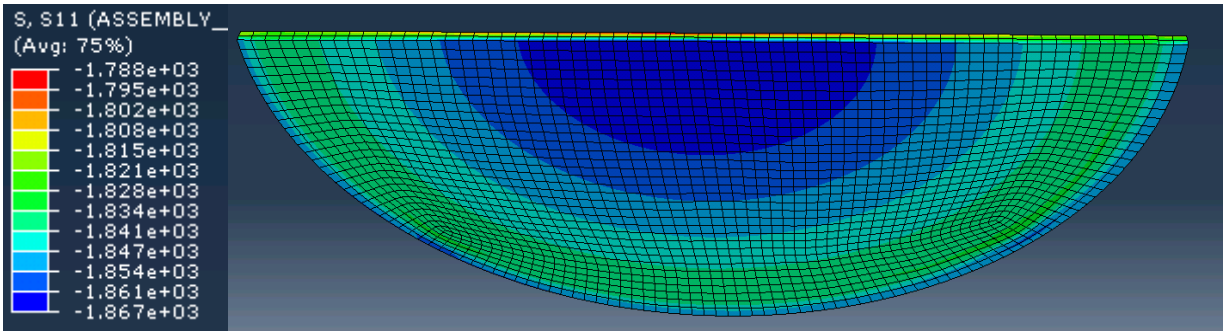

Fig. 4.33-Localized maximum normal compressive stresses in the electrolyte following the heating cycle from 20 - 350°C, in the radial σ_{11} direction.

References Cited

1. ASTM Standard B209-14, “Standard Specification for Aluminum and Aluminum-Alloy Sheet and Plate,” ASTM International, West Conshohocken, PA, 2014.

Chapter 5 – Summary

As the world constantly evolves and the dependence of reliable energy is increased, the implementation of sustainable, safe, and economically feasible routes of storing large concentrations of energy will without a doubt be required. The energy storage technology reported in this work sheds light on an early solution to this impending dilemma. Not only can this technology harness large amounts of energy created by traditional means, but it can also be used to legitimize the incorporation of newer "clean-energy" sources, by utilizing the excess energy when it is available, and releasing it later when required. A feat up until recently was not possible.

As the advancement of computational numerical methods has improved in recent years, FEA analysis has become an essential, cost effective tool for design evaluation and optimization. The NaS secondary cell is no exception, and the work provided here has proven the methods competency in analyzing the complexities not otherwise possible using traditional means.

In this study, FEA computational techniques were employed to reliably predict the localized stress distributions within the planar-type NaS cell. The developed FEA models aided in determining how variations in both material properties and geometrical changes can influence the resultant thermally induced stress concentrations. From the results it was concluded that changes in both the CTE values and thickness of the outer cell container had the largest influences in the resultant localized stress distributions within the rigid, non-elastic ceramic components of the cell. It was further determined that the electrolyte centering during the fabrication process is of great concern, as non-symmetric stress

distributions resulted from this investigation, placing higher stresses at the smaller GS cross-section. The following address the limitations, findings, and future research directions of the current thesis.

5.1 Limitations

- The material properties incorporated in the model development were completely homogenous within the constituent parts.
- The exothermic and endothermic chemical reaction influences were not included in the temperature profiles of computations.
- Computations were conducted based on idealized/simplified cell geometry.

5.2 Findings

- 3D FEA modeling was conducted to predict the stress distributions at the various components of the planar-type NaS battery cell, based upon induced thermal loading.
- The localized maximum normal and shear stresses in the cell joint areas and electrolyte were identified and the resultant stress concentrations were quantified.
- In the standard cell with the electrolyte diameter of 120mm, the location of highest localized normal stress was induced at the outer surface of the insulating header after the initial cooling cycle. The overall highest localized compressive stresses were identified on the lower surface of the electrolyte, near the center of the cell after the heating (thaw) cycle. The highest resultant

shear stresses within the cell were identified at the lower insulating header surface after the cell assembly. Significant normal compressive stresses were identified at all of the insulating header surfaces after the heating (thaw) cycle. In the standard cell, the upper and lower insert metals experienced the highest compressive stresses after the final cooling (freeze) cycle.

- Varying the glass-sealing CTE value did not yield significant stress concentration differences.
- As the CTE values of the container materials were decreased closer to those of the centrally located ceramics, the normal and shear stress concentrations were significantly lowered at all locations except the innermost glass-sealing, which was minimal.
- By lowering the average container CTE values to an average of $9E^{-5}K^{-1}$ from $11E^{-5}K^{-1}$, the resultant outer insulating header normal stress was reduced by nearly half. The reduction in the measured normal and shear stresses in the insert metals over the same container CTE variance was approximately half as well.
- Reducing the thickness of the upper and lower Al insert metals did not yield significant stress concentration differences.
- Changing the outer container thickness induced the most significant differences among all trials. The outermost localized normal stresses on the insulating header were reduced by nearly 100MPa when the container material thickness was reduced by 25%, and increased by nearly 100MPa when the container material thickness was increased by 25%. Similar

significant localized normal stresses at the insulating header-upper insert metal interface were also evident when the container thickness was varied.

- Centering of the electrolyte during synthesis is of valid concern. Off-setting the electrolyte by 50% induced significant deflection of the stress concentrations in both the normal and shear stress directions. Less accumulated radial compressive stresses were evident at the thicker portion of the glass-sealing when compared with similar locations at the thinner portions of the glass-sealing. An increase in the upper normal stresses on the glass-sealing were also evident at the thinner portion of the glass-sealing.

5.3 Future Research

- Exploration into the fracture mechanics (such as brittle fracture using Griffith criteria) in the cell joint areas/electrolyte could be implemented to determine if the stress accumulations identified, could cause potential failure mechanisms to occur.
- The developed models could be applied to predict the thermomechanical stress concentrations for other NaS systems with different potential designs and material types/pairs. This will guide in the development of a more stable and safe NaS battery system.
- The developed macroscopic model can be extended to a multi-scale model focusing on the interface structures in the cell joints.
- The developed models could be used to explore additional/different temperature cycling profiles.